SPECIAL
PECAN
COLLECTION

Composite In Situ Microphysical Analysis of All Spiral Vertical Profiles Executed within BAMEX and PECAN Mesoscale Convective Systems

DANIEL M. STECHMAN[a]

Department of Atmospheric Sciences, University of Illinois at Urbana–Champaign, Urbana, Illinois, and Cooperative Institute for Mesoscale Meteorological Studies, University of Oklahoma, and NOAA/OAR/National Severe Storms Laboratory, Norman, Oklahoma

GREG M. MCFARQUHAR

Cooperative Institute for Mesoscale Meteorological Studies, and School of Meteorology, University of Oklahoma; Norman, Oklahoma

ROBERT M. RAUBER AND BRIAN F. JEWETT

Department of Atmospheric Sciences, University of Illinois at Urbana–Champaign, Urbana, Illinois

ROBERT A. BLACK

NOAA/OAR/Atlantic Oceanographic and Meteorological Laboratory, Miami, Florida

(Manuscript received 13 November 2019, in final form 13 May 2020)

ABSTRACT

Vertical profiles of temperature, relative humidity, cloud particle concentration, median mass dimension, and mass content were derived using instruments on the NOAA P-3 aircraft for 37 spiral ascents/descents flown within five mesoscale convective systems (MCSs) during the 2015 Plains Elevated Convection at Night (PECAN) project, and 16 spiral descents of the NOAA P-3 within 10 MCSs during the 2003 Bow Echo and Mesoscale Convective Vortex Experiment (BAMEX). The statistical distribution of thermodynamic and microphysical properties within these spirals is presented in context of three primary MCS regions—the transition zone (TZ), enhanced stratiform rain region (ESR), and the anvil region (AR)—allowing deductions concerning the relative importance and nature of microphysical processes in each region. Aggregation was ubiquitous across all MCS zones at subfreezing temperatures, where the degree of ambient subsaturation, if present, moderated the effectiveness of this process via sublimation. The predominately ice-supersaturated ESR experienced the least impact of sublimation on microphysical characteristics relative to the TZ and AR. Aggregation was most limited by sublimation in the ice-subsaturated AR, where total particle number and mass concentrations decreased most rapidly with increasing temperature. Sublimation cooling at the surface of ice particles in the TZ, the driest of the three regions, allowed ice to survive to temperatures as high as +6.8°C. Two spirals executed behind a frontal squall line exhibited a high incidence of pristine ice crystals, and notably different characteristics from most other spirals. Gradual meso- to synoptic-scale ascent in this region likely contributed to the observed differences.

1. Introduction

Despite the demonstrated importance of microphysical processes within MCSs, in situ cloud microphysical observations within such systems are rare. The first such observations were collected during a spiral descent of the National Oceanic and Atmospheric Administration (NOAA) P-3 aircraft through the stratiform region of the 10–11 June 1985 squall line observed as a part of the Preliminary Regional Experiment for STORM-Central

Supplemental information related to this paper is available at the Journals Online website: https://doi.org/10.1175/JAS-D-19-0317.s1.

[a] Current affiliations: Cooperative Institute for Mesoscale Meteorological Studies, University of Oklahoma, and NOAA/OAR/National Severe Storms Laboratory, Norman, Oklahoma.

Corresponding author: Daniel M. Stechman, stechman@ou.edu

DOI: 10.1175/JAS-D-19-0317.1

(PRE-STORM; Cunning 1986). Additional observations were obtained during the 2003 Bow Echo and Mesoscale Convective Vortex Experiment (BAMEX; Davis et al. 2004), the 2011 Midlatitude Continental Convective Clouds Experiment (MC3E; Jensen et al. 2016), and the Plains Elevated Convection at Night (PECAN; Geerts et al. 2017) project.

PECAN targeted observations of nocturnal MCSs over the Great Plains of the United States during June and July 2015. The P-3 was employed, as in BAMEX, to make in situ thermodynamic and microphysical observations as well as airborne radar observations from the NOAA tail Doppler radar (TDR) across nine MCSs, five of which had at least one spiral ascent or descent (henceforth referred to as spiral profiles) conducted within. Stechman et al. (2020, hereafter S20) provide an in-depth analysis of the 20 June 2015 PECAN MCS, which included spiral profiles executed in the vicinity of the rear inflow jet (RIJ) of the MCS, and within each of the three regions common to the leading-line–trailing stratiform MCS archetype (e.g., Houze et al. 1989; Parker and Johnson 2000). These MCS regions include the enhanced stratiform region (ESR), commonly associated with a broad area of relatively continuous light to moderate precipitation reaching the surface, the transition zone (TZ), an area of weak reflectivity separating the ESR from the convective line, and the anvil region (AR), characterized by predominately ice clouds and little to no precipitation reaching the surface. S20 found aggregation was common in each MCS zone, with modification by sublimation deduced to have varying degrees of importance as dependent upon ambient subsaturation. Observations within the TZ coincident with the RIJ revealed that ice was present at temperatures as high as +6.8°C, likely due to enhanced descent within the RIJ and sublimation/evaporative cooling.

The present study builds upon the analyses of the BAMEX in situ microphysics observations presented by McFarquhar et al. (2007a, hereafter M07), Smith et al. (2009, hereafter SM09), and Grim et al. (2009a, hereafter G09, 2009b) by combining them with those from PECAN under a common conceptual and analysis framework. The spiral profiles from S20 are considered along with spirals from four other PECAN MCSs, and 10 BAMEX MCSs previously discussed, yielding a total of 53 spirals for analysis. Details concerning the collection, processing, and analyses of these observations are provided in section 2, results of the statistical analyses are presented in section 3, with a discussion of the results and conclusions provided in section 4.

2. Data sources and methods

This study uses airborne in situ thermodynamic and cloud microphysics data collected aboard the NOAA P-3 during the 2015 PECAN and 2003 BAMEX field campaigns. The airborne in situ data from BAMEX were reprocessed for the present study to take advantage of improvements in processing techniques over the past 15 years, including the identification and removal of shattered ice crystal artifacts (e.g., Korolev and Isaac 2005; McFarquhar et al. 2007b, 2011; Jackson et al. 2014), and to allow for uniform comparisons with the PECAN data, including the use of a common set of habit-dependent mass–diameter relationships (Jackson et al. 2012, 2014). In situ observations were analyzed in the context of MCS structure using observations from the P-3 TDR as well as from the ground-based Weather Surveillance Radar-1988 Doppler (WSR-88D) network. Details concerning the acquisition and processing of these observations, as well as the conceptual framework in which analyses were considered, are provided in this section.

a. Radar observations

The TDR is a 3.22-cm wavelength X-band Doppler radar with two separate conically scanning antennas, angled 20° fore and aft of the P-3, which yields pseudovertical cross sections of radar reflectivity and radial velocity. For each PECAN mission, observations from WSR-88Ds in the vicinity of the analyzed MCS were combined using the Python ARM Radar Toolkit (Py-ART; Helmus and Collis 2016) to provide composites of radar reflectivity at 1 km above ground level (AGL). The P-3 flight track was overlaid on these composites, as well as maximum range (71.38 km) indicators for the fore and aft beams of the TDR. Combining these composites with coincident TDR observations allowed for the diagnosis of each MCS type and of the location of each spiral relative to common MCS structure and organization. Further details concerning the characteristics and processing of the PECAN TDR and WSR-88D data are given by S20. The SM09 BAMEX study used TDR data and WSR-88D composites in a similar fashion, details of which are provided therein.

b. Thermodynamic and microphysical observations and processing

Flight-level thermodynamic observations from BAMEX and PECAN were processed using a common methodology, as described by S20, yielding temperature determined using the Zipser et al. (1981) sensor wetting correction (T), and flight-level relative humidity (RH) with respect to water (RH_w) for $T > 0$°C and ice (RH_i) for $T \leq 0$°C. Any references to RH with no subscript refer to the entire RH profile (inclusive of both RH_w and RH_i).

A Droplet Measurement Technologies (DMT) cloud imaging probe (CIP), precipitation imaging probe (PIP) and cloud droplet probe (CDP) were installed on the P-3 during PECAN to measure cloud and precipitation

particle properties. The CDP is a forward scattering probe that provides information on liquid cloud droplets for particles with diameters between 1 and 50 μm. The CIP and PIP are optical array probes (OAPs) with 64 sizing elements of 25- and 100-μm resolution, respectively. The PIP data were unusable due to a malfunction of the probe, thus limiting the observable range of particle maximum dimension (D; diameter of smallest circle enclosing each particle; Wu and McFarquhar 2016) to that of the CIP, which is 125 μm to approximately 2 mm. Particle size distributions (PSDs) for particles covering D up to 12 mm were estimated by forcing mass closure between observations of the bulk total water content (TWC) from the Science Engineering Associates Inc., multielement water content system (WCM-2000; Strapp et al. 2008) and that derived from the PSDs. The TWC was determined from the CIP and the estimated PSDs using a combination of habit-dependent mass–diameter relationships (Jackson et al. 2014) and a mass–diameter relationship appropriate for an MCS trailing stratiform region (Finlon et al. 2019). Full details concerning the processing of the PECAN cloud microphysics data, as well as the reprocessing of the BAMEX Particle Measurement Systems (PMS) two-dimensional cloud (2DC) and precipitation (2DP) probe data are provided by S20. As in S20, BAMEX 2DC data for $D < 1$ mm were combined with 2DP data for $D \geq 1$ mm yielding combined PSDs spanning the range 150 μm to 6.8 mm.

This study primarily focuses on analyses of bulk cloud properties calculated from the PECAN and BAMEX PSDs, including total number concentration (N_t), TWC, and median mass diameter (D_{mm}). Additionally, T of melting onset and completion was determined through inspection of particle imagery. Particle images representative of each 1°C increment within each spiral were used to subjectively identify vertical variability of hydrometeor morphology. The variability of particle shape was also computed quantitatively using averages of particle area ratios ($\mathscr{A}$; McFarquhar and Heymsfield 1996), where $\mathscr{A}$ is defined as the projected area of a particle divided by the area of a circle with diameter D.

Observations of liquid PSDs for $1 \leq D \leq 50$ μm from a PMS forward-scattering spectrometer probe (FSSP) during BAMEX, and from the CDP during PECAN were used to provide an indication of the presence of supercooled liquid water (SLW). Following Heymsfield et al. (2011) and Finlon et al. (2019), it is assumed that all time periods with CDP/FSSP concentrations greater than 10 cm^{-3} at $T \leq 0$°C corresponded to the presence of SLW.

c. Conceptual framework

To aid in the interpretation and analysis of the microphysical and thermodynamic vertical profiles, PECAN TDR observations and WSR-88D composites were used to classify spirals based on their location relative to key MCS regions, including the TZ, ESR, and the AR. Results of these classifications were combined with the SM09 BAMEX spiral classifications to create a larger dataset. Traditionally these regions are discussed in the context of the leading-line–trailing-stratiform (TS) MCS archetype (Parker and Johnson 2000), though in the interest of uniformity and inclusion of most spirals they have been extended where appropriate for use with the parallel stratiform (Parker and Johnson 2000) and nonlinear system (Gallus et al. 2008) archetypes. Spirals were determined to be in the TZ if they occurred in the region of relatively weak reflectivity (<~20 dBZ) or no radar echo bounded by the convective line and the ESR and/or AR, where little to no precipitation was reaching the surface. The ESR was identified by the presence of a wide area of fairly contiguous reflectivity between ~20–35 dBZ extending to the surface, often accompanied by a radar bright band signifying the location of the melting layer, indicated by a horizontal band of locally enhanced reflectivities typically 35–45 dBZ. The AR was considered to be any region on the periphery of the MCS characterized by primarily ice clouds, with any precipitation either sublimating or evaporating before reaching the surface. Note that the AR is inclusive of the rear anvil region of the leading-line–trailing-stratiform MCS archetype, and fringes of the convective line in the parallel stratiform archetype. The location of each BAMEX and PECAN spiral analyzed in this study is provided relative to the MCS archetypes in Fig. 1.

Flight-level wind speeds from each spiral were used to determine whether there was a transect through an RIJ, typically indicated by values in excess of 20 m s^{-1} (not shown). The TDR radial velocities were inspected for spirals meeting this criterion to confirm the expected location, extent, and orientation of the strongest winds relative to the leading-line–trailing-stratiform MCS archetype. All TZ spirals and six ESR spirals occurred near or within the axis of the RIJ allowing analysis and comparison of the environments within and removed from this important feature.

The 53 spiral profiles considered in this study were executed across 10 BAMEX missions and five PECAN missions. Brief overviews of each analyzed BAMEX and PECAN P-3 intensive operation period (IOP) and unofficial field operation (UFO) are given in the appendix to provide a meteorological basis for how each system formed and evolved, along with any operational/logistical information of relevance to the present study.

The characteristics of the first two spirals from the 6 July 2015 PECAN mission, within stratiform precipitation of postfrontal convection, and the 24 May 2003

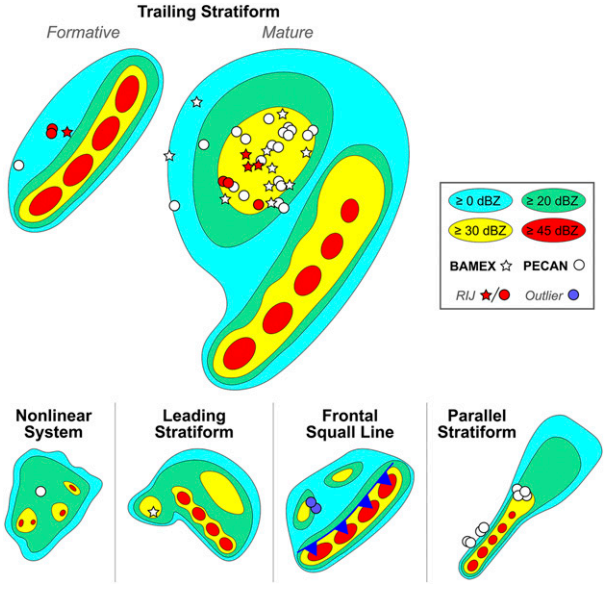

FIG. 1. Idealized representation of MCS structures [partially adapted from Parker and Johnson (2000) and Gallus et al. (2008)]. Symbols indicate the general locations of spiral profiles executed during BAMEX and PECAN. Red symbols indicate the given spiral occurred within or near the axis of the RIJ, while blue symbols represent outlier spirals excluded from the primary MCS zone analysis.

BAMEX spiral, behind the center of a mesoscale convective vortex (MCV), were notably different than the spirals in the main analysis set. These outlier spirals were thus considered separately.

Building upon the scheme SM09 used to analyze the BAMEX data, the 37 PECAN spirals and 16 BAMEX spirals were segregated into two analysis groups: 1) 50 spirals within the three primary MCS zones, namely, the TZ, ESR, and AR, including a comparison of ESR spirals within or near the RIJ and those removed from the main impacts of the RIJ, and 2) 3 spirals exhibiting atypical characteristics. Statistical analyses of spirals in these groups are presented in the following sections.

d. Statistical analyses

The primary dataset analyzed in this study is derived from observations collected during 50 spiral profiles: 15 from BAMEX and 35 from PECAN. Data from each spiral were combined into three aggregate datasets depending upon whether the spiral occurred in the TZ, ESR, or AR, with two additional aggregate datasets for ESR spirals within or near the RIJ, and ESR spirals removed from the main impacts of the RIJ.

For each aggregate dataset, the median and 25th and 75th percentiles were calculated within 1°C T bins for each of the following microphysical properties: RH, N_t, TWC, $D_{\rm mm}$, and $\mathscr{A}$, where the temperature-dependent medians are given by $\widetilde{\mathbf{RH}}$, $\widetilde{N_t}$, $\widetilde{\mathbf{TWC}}$, $\widetilde{D_{\rm mm}}$, and $\widetilde{\mathscr{A}}$, respectively. The average rates of change of $\widetilde{\mathbf{RH}}$, $\widetilde{D_{\rm mm}}$, and $\widetilde{\mathscr{A}}$ relative to T within each MCS region were computed using a linear least squares fit to data acquired above and below the melting layer, separately. Following the approach of M07, fractional rates of change with respect to T of $\log_{10}\widetilde{N_t}$ and $\log_{10}\widetilde{\mathbf{TWC}}$ were derived from linear least squares fits to those quantities.

The CDP and FSSP observations of N_t at $T \le 0$°C were sorted into 1°C bins for each zone within the MCS. The percentage of observations identified as liquid water using the aforementioned 10-cm^{-3} concentration threshold within each T bin of each region was calculated to provide an indication of the relative incidence of SLW as a function of T.

Differences between the temperature-dependent quantities in the different regions were quantified using the two-sample Kolmogorov–Smirnov (K-S) test. The K-S test compares two data samples with a null hypothesis that the two samples were drawn from the same underlying continuous distribution, and the nature of said distribution need not be known. The K-S test was performed separately for data within each 1°C T bin if and only if that bin consisted of at least five valid values for each of the two samples. The null hypothesis was rejected, with differences between a given set of samples deemed significant, for p values less than a significance level of 0.05.

In cases where an analysis set consisted of fewer than three spirals, as with the outlier postfrontal spirals, vertical profiles of the 10-s averages of each quantity were used in the analysis. Layer-average values and rates of change were computed for each variable in each spiral directly, not from the binned median values as with the aggregate datasets, and the K-S test was not performed. These and the other quantities introduced here are presented in section 3.

3. MCS zone comparisons

A total of 50 spirals, 35 from PECAN and 15 from BAMEX, were categorized by MCS zone yielding 3 in the TZ, all within the rear inflow notch, 39 in the ESR (including 6 within the RIJ), and 8 in the AR. The MCS zone, beginning and ending time and altitude, maximum and minimum T and RH, T of the melting-layer top and bottom (when observed), the average rate of change of T with respect to altitude, and the fractional rates of change with respect to T of $\log_{10}N_t$ and $\log_{10}$TWC for $T \le 0$°C (determined following the approach described in section 2d) of each BAMEX and PECAN spiral considered in this study are provided in Table S1 in the online supplemental material.

Graphical representations of how the medians and 25th–75th-percentile spreads of RH, N_t, TWC, $D_{\rm mm}$, and

TABLE 1. The average (denoted by overbars, $\overline{\cdots}$) median values and rates of change of the median with increasing T of RH, N_t, TWC, D_{mm}, and $\mathscr{A}$ for the TZ, ESR, AR, ESR-RIJ (E-RIJ), and ESR non-RIJ (E-NRIJ) above ($T \leq 0$°C) and below ($T \geq +5$°C) the melting layer. All values associated with RH are with respect to ice for $T \leq 0$°C and with respect to liquid water for $T \geq +5$°C.

	$T \leq 0$°C					$T \geq +5$°C				
	MCS zone					MCS zone				
	TZ	ESR	AR	E-RIJ	E-NRIJ	TZ	ESR	AR	E-RIJ	E-NRIJ
RH										
$\overline{\widetilde{\mathbf{RH}}}$ (%)	97.3	106.9	94.4	106.3	106.2	40.8	66.3	61.7	67.0	67.0
$d\overline{\widetilde{\mathbf{RH}}}/dT$ (% °C^{-1})	−3.1	−1.2	−1.4	−1.3	−1.2	−3.1	−3.3	−2.0	−3.0	−3.3
N_t										
$\overline{\widetilde{N}_t}$ (cm^{-3})	1.92×10^{-2}	4.20×10^{-2}	1.64×10^{-2}	5.98×10^{-2}	3.88×10^{-2}	4.80×10^{-4}	4.91×10^{-4}	3.80×10^{-4}	1.10×10^{-3}	4.33×10^{-4}
$d \log \widetilde{N}_t/dT$ (% °C^{-1})	−24.7	−20.5	−28.9	−23.4	−20.7	−45.2	−19.4	−40.6	−4.0	−19.1
TWC										
$\overline{\widetilde{\mathbf{TWC}}}$ (g m^{-3})	0.472	0.666	0.419	0.800	0.636	0.052	0.120	0.166	0.329	0.113
$d \log\overline{\widetilde{\mathbf{TWC}}}/dT$ (% °C^{-1})	−11.5	−11.5	−15.9	−16.4	−11.3	−87.2	−16.5	−72.5	+0.0	−16.6
D_{mm}										
$\overline{\widetilde{\boldsymbol{D}}_{mm}}$ (mm)	2.503	2.102	2.108	1.977	2.150	0.765	1.783	1.163	1.497	1.798
$d\widetilde{\boldsymbol{D}}_{mm}/dT$ (μm °C^{-1})	+180	+136	+132	+108	+150	−126	−36	−114	−19	−31
$\mathscr{A}$										
$\overline{\widetilde{\mathscr{A}}}$ (%)	46.8	45.1	47.5	45.6	44.9	57.3	68.8	67.7	68.1	69.2
$d\widetilde{\mathscr{A}}/dT$ (% °C^{-1})	−0.18	−0.20	−0.01	−0.16	−0.21	+1.30	+0.24	+1.72	+0.14	+0.22

TABLE 2. The average values (denoted by overbars, $\overline{\cdots}$) and rates of change with increasing T of RH, N_t, TWC, D_{mm}, and $\mathscr{A}$ for the two PECAN postfrontal spirals above ($T \leq 0$°C) the melting layer and for the second postfrontal spiral alone below ($T \geq +5$°C) the melting layer. All values associated with RH are with respect to ice for $T \leq 0$°C and with respect to liquid water for $T \geq +5$°C.

	$T \leq 0$°C		$T \geq +5$°C
	Post–front 1	Post–front 2	Post–front 2
RH			
$\overline{\mathrm{RH}}$ (%)	104.3	100.8	73.9
$d\mathrm{RH}/dT$ (% °C^{-1})	−1.5	−1.7	−0.3
N_t			
$\overline{N_t}$ (cm^{-3})	1.21E-02	9.39E-03	4.51E-04
dN_t/dT (% °C^{-1})	+32.8	+16.8	−6.2
TWC			
$\overline{\mathrm{TWC}}$ (g m^{-3})	0.215	0.288	0.025
$d\mathrm{TWC}/dT$ (% °C^{-1})	+28.1	−6.2	−0.2
D_{mm}			
$\overline{D_{mm}}$ (mm)	3.332	4.048	1.070
dD_{mm}/dT (μm °C^{-1})	−39	−263	+74
$\mathscr{A}$			
$\overline{\mathscr{A}}$ (%)	50.0	49.7	70.1
$d\mathrm{A}/dT$ (% °C^{-1})	−1.72	+0.08	+0.67

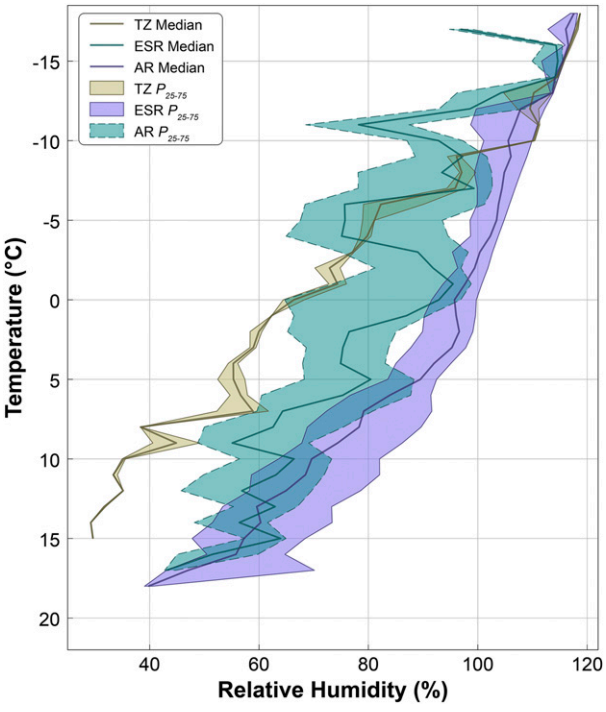

FIG. 2. Vertical profiles of $\widetilde{\mathbf{RH}}$ (%; tan, blue, and green solid lines) and the 25th–75th-percentile range of RH (%;tan, blue, and green shading) for the TZ, ESR, and AR MCS zones as a function of T (°C). RH is with respect to ice for $T \leq 0$°C and with respect to liquid water for $T > 0$°C.

$\mathscr{A}$ varied as a function of T within each MCS zone are presented in this section. As detailed in section 2d, the temperature-dependent median values and the average rates of change of those as a function of T were analyzed both above and below the melting layer (Table 1), with the melting layer defined here as $0° < T < +5$°C for the purposes of multispiral comparison. The postfrontal spirals were considered in a similar fashion, though with averages and average rates of change calculated over all data in each 1°C T bin (Table 2). Due to the non-Lagrangian nature of the spirals, specific processes affecting individual particle populations cannot be observed. However, information about the processes occurring in the regions sampled by these spirals can be inferred by considering the rates of change of microphysical quantities as a function of T, and the types of particles and conditions present.

a. Enhanced stratiform region

The RH_i observed within the ESR was at or above ice saturation for $T \leq -6$°C in 27 of the 39 spirals (Fig. 2), with an average $\widetilde{\mathbf{RH}}_i$ for $T \leq 0$°C of 107% (Table 1). Changes in the ESR PSDs above the melting layer were consistently characterized by greater decreases in $\log N_t$ than in logTWC (Table 1 and Table S1). These characteristics were reflected in the median profiles of $\boldsymbol{N}_t$ and **TWC** (Figs. 3 and 4), with $d\log\widetilde{\boldsymbol{N}_t}/dT = -20.5\%$ °C^{-1} and $d\log\widetilde{\mathbf{TWC}}/dT = -11.5\%$ °C^{-1} (Table 1). In the absence of factors such as diffusional growth or sublimation, aggregation results in a decrease of N_t with increasing T as particles combine to produce fewer, larger particles. As aggregates grow in size, their fall speeds increase yielding further reductions of N_t while also reducing TWC (e.g., Field and Heymsfield 2003; Field et al. 2006; Brandes et al. 2007; M07; Brandes et al. 2008; G09). Thus, aggregation alone is expected to produce greater fractional rates of decrease in N_t than TWC. When subsaturated conditions are present, most prevalent in the TZ and AR spirals, further decreases in N_t than TWC are driven by sublimation, which favors the removal of smaller particles (Gu and Liou 2000) and the reduction in size of larger particles.

The expected increase in particle size from aggregation with increasing T just above the melting layer is seen via a $d\widetilde{\boldsymbol{D}_{mm}}/dT$ of +136 μm °C^{-1} (Fig. 5; Table 1), with a predominance of aggregates observed in the particle imagery. Examining individual ESR spiral profiles (not shown), an increase in D_{mm} with increasing T above the melting layer was seen during all but two BAMEX spirals (spiral 1 on 5 July, and spiral 2 on 29 June), and all but three PECAN spirals (spirals 5–7 on 17 June). These exceptions were in regions of weaker stratiform precipitation, and were generally associated with higher values of RH_i and N_t relative to most other ESR spirals. The reasons for the different

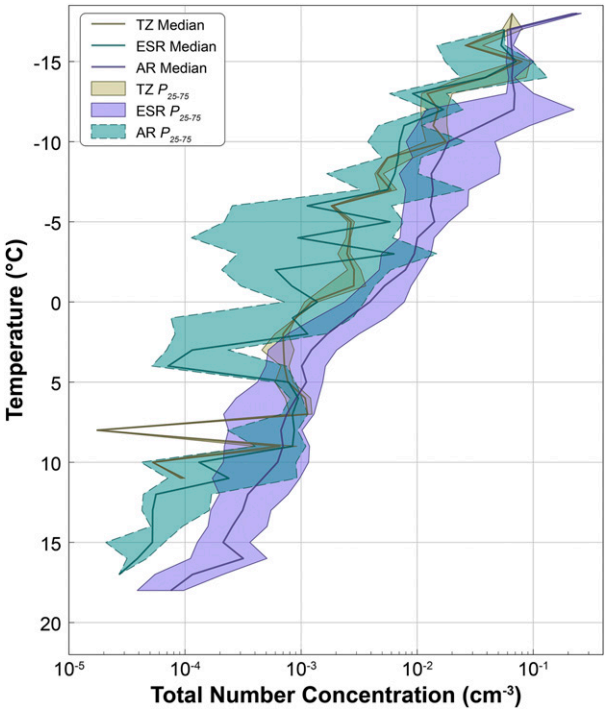

FIG. 3. As in Fig. 2, but for N_t (cm^{-3}).

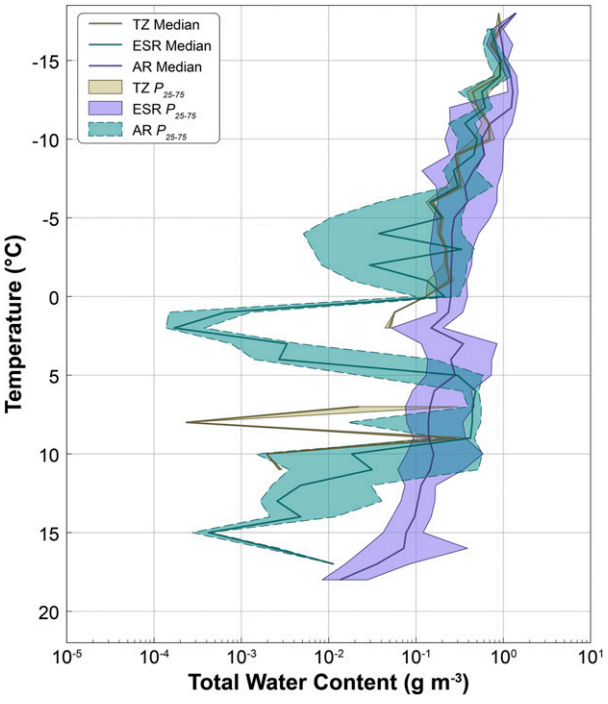

FIG. 4. As in Fig. 2, but for TWC (g m^{-3}).

behavior observed during those spirals are not currently known.

Vertical profiles of $\mathscr{A}$ are useful in identifying possible aggregation events and the temperatures where melting is occurring. As ice particles melt and collapse into water drops, values of $\mathscr{A}$ rapidly increase as the particle shape becomes more circular. Conversely, when particles aggregate into more spatially open and irregular shapes, $\mathscr{A}$ would be expected to decrease. The most negative $d\widetilde{\mathscr{A}}/dT$ among the MCS zones at and above the melting layer was observed in the ESR, at −0.2% °C^{-1} for $T \leq 0$°C (Fig. 6; Table 1). In addition, the lowest average $\widetilde{\mathscr{A}}$ for $T \leq 0$°C (−45.1%) was also associated with the ESR, suggesting aggregation was most dominant there relative to the TZ and AR. However, in the ESR spirals where melting onset occurred at or near 0°C, there was no evidence of an increase in the rate of aggregation just above the melting layer, a process previously illustrated by Biggerstaff and Houze (1991, 1993) and M07. The absence of an increased rate of aggregation in these spirals is not presently understood.

Examination of individual spiral profiles showed that a subset of seven ESR spirals had delays in the onset of melting to +2.5°C on average. For those spirals, $\mathscr{A}$ decreased more rapidly with increasing T, up to −1% °C^{-1} for $T < +2.5$°C, ranging from 28% to 45% near the top of the melting layer. The regions in which these spirals were executed were slightly drier compared to the other ESR spirals, with RH_i at $T = 0$°C ranging from 80% to 95% for the melting delay spirals, compared to 80%–100% in the other ESR spirals. As with most other ESR spirals, D_{mm} increased toward the melting layer in these seven spirals. Thus, the increase in D_{mm} and decrease in $\mathscr{A}$ observed in the regions where these spirals were conducted may indicate aggregation was occurring more actively just above and possibly within the melting layer than farther above, with the observed delay in melting onset likely due to sublimational cooling at the surface of the ice particles in the subsaturated air.

Analysis of the CDP and FSSP N_t over all ESR spirals revealed that SLW was sometimes present, with the percentage of observations exceeding the 10-cm^{-3} threshold increasing from 1% at −10°C to a peak of 16% at −2°C (Fig. 7). Although the ESR particle images did not definitively indicate the presence of graupel, it is expected that riming was at least partially responsible for particle growth for $T > -5$°C for some time periods.

Taken together, these results indicate that for $T \leq 0$°C in the ESR, aggregation served as the dominant microphysical process controlling the evolution of particle shapes and sizes. The values of RH_i near ice saturation above the melting layer for most spirals further suggest that the influence of sublimation on depositional growth would be minimal.

As previously noted, 31% of all ESR spirals were collected within the 9 July 2015 PECAN MCS. Data from

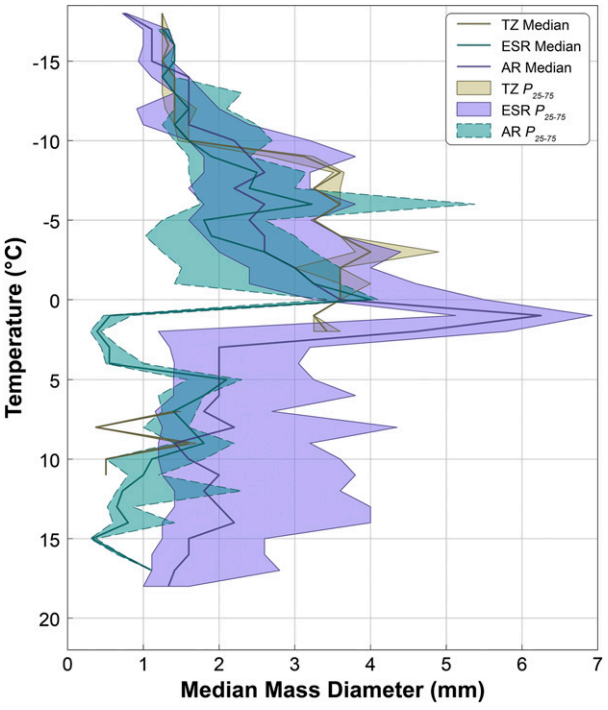

FIG. 5. As in Fig. 2, but for D_{mm} (mm).

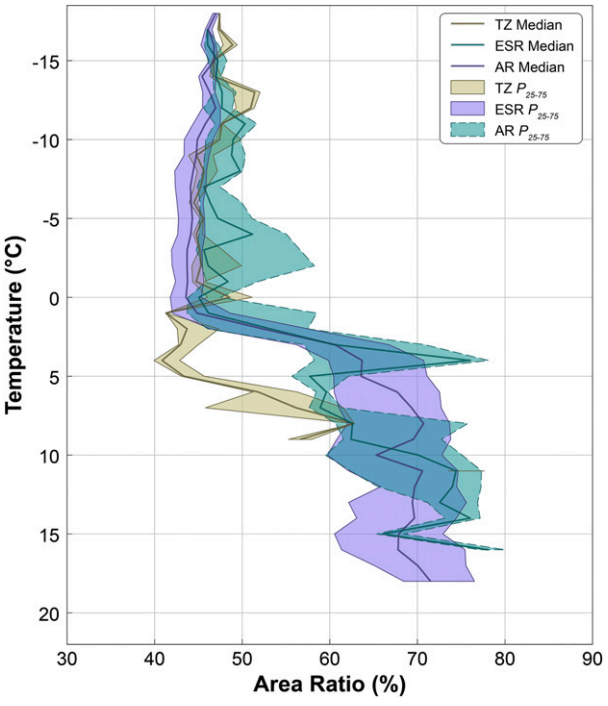

FIG. 6. As in Fig. 2, but for $\mathscr{A}$ (%).

this case thus dominate the statistical distributions within the vertical profiles presented herein, with generally drier conditions in the 9 July ESR spirals, along with lower N_t, higher ice water contents and lower liquid water contents, and a greater D_{mm} than within spirals conducted on other days. Though the degree to which this impacts the conclusions of this study is not known, the combined ESR statistics are expected to be representative of the wide range of conditions and characteristics found in the ESR of MCSs.

b. *Transition zone*

The three TZ spirals were combined in a single classification set for comparison with the ESR and AR sets, noting that observations were limited to $-9.3° \le T \le -17.6°\mathrm{C}$ and $+15.4° \le T \le -17.6°\mathrm{C}$ for the first and second spirals of the 20 June PECAN MCS, respectively, and $+9.2° \le T \le -9.3°\mathrm{C}$ for the first spiral of the 29 June BAMEX spiral. Of note, any gradients in the key quantities between the observations at the top of spiral 1 of 29 June and bottom of spiral 1 of 20 June, around −9.3°C, were generally reflected in the spiral 2 observations of 20 June (not shown). As such, gradients in the TZ statistical quantities for $-9° \ge T \ge -10°\mathrm{C}$ are not thought to be artifacts.

The TZ average $\widetilde{\mathbf{RH}}_i$ for $T \le 0°\mathrm{C}$ was 97% (Table 1), with ice-saturation for $T < -9°\mathrm{C}$ (Fig. 2). The TZ environment rapidly dried with T for $T > -9°\mathrm{C}$, with a $d\widetilde{\mathbf{RH}}/dT$ of $-3.1\%\ °\mathrm{C}^{-1}$, $\widetilde{\mathbf{RH}}_i$ of 65% at $T = 0°\mathrm{C}$, and $\widetilde{\mathbf{RH}}_w$ decreasing to 30% at $T = +15°\mathrm{C}$. The TZ was by far the driest of the MCS zones for $T > -4°\mathrm{C}$, with a similar moisture profile to the AR for $-4° \ge T \ge -9°\mathrm{C}$ and the ESR for $T < -9°\mathrm{C}$.

Greater decreases in $\log\widetilde{\boldsymbol{N}}_t$ than in $\log\widetilde{\mathbf{TWC}}$ with increasing T were observed in the TZ for $T \le 0°\mathrm{C}$ (Figs. 3 and 4), with a $d\log\widetilde{\boldsymbol{N}}_t/dT$ of $-24.7\%\ °\mathrm{C}^{-1}$ and $d\log\widetilde{\mathbf{TWC}}/dT$ of $-11.5\%\ °\mathrm{C}^{-1}$ (Table 1). Over the same range of T, $d\widetilde{\boldsymbol{D}}_{\mathrm{mm}}/dT$ was $+180\,\mu\mathrm{m}\,°\mathrm{C}^{-1}$ (Table 1), with a localized trend of greater magnitude for $-10° < T < -8°\mathrm{C}$ and relatively constant values above and below (Fig. 5). The localized jump in $\widetilde{\boldsymbol{D}}_{\mathrm{mm}}$ at $-10° < T < -8°\mathrm{C}$ was primarily influenced by spiral 2 of 20 June, where an increase in D_{mm} of $+955\mu\mathrm{m}\ °\mathrm{C}^{-1}$ for $-13° < T < -8°\mathrm{C}$ was observed in conjunction with CDP observations of N_t exceeding $300\,\mathrm{cm}^{-3}$ (not shown) indicating SLW. A spike in the percentage of TZ CDP/FSSP N_t observations suggesting the presence of SLW was seen within this same layer (Fig. 7), because of data collected during the 20 June spiral 2. As such, riming likely contributed to the enhanced particle growth observed over $-10° < T < -8°\mathrm{C}$ within that spiral, though it is unclear whether this is a general characteristic of the TZ.

As discussed in the previous section, vertical profiles of $\mathscr{A}$ are helpful in quantifying changes in particle morphology and in objectively confirming particle

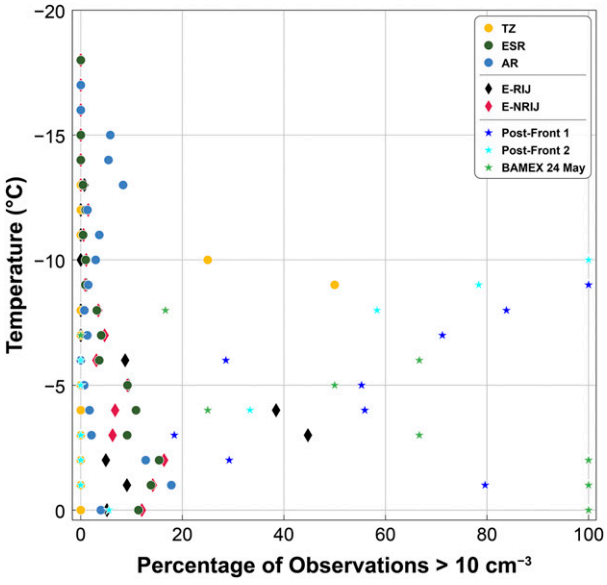

FIG. 7. Percentage of CDP and FSSP observations of N_t exceeding 10 cm^{-3} as a function of T (°C). The yellow, green, and blue circles correspond to the TZ, ESR, and AR observations, respectively. The black and red diamonds represent ESR observations in the vicinity of the RIJ (E-RIJ), and non-RIJ (E-NRIJ) observations, respectively. The stars correspond to the two PECAN post-frontal spirals from 6 Jul 2015 (blue and cyan) and the BAMEX MCV spiral from 24 May 2003 (green).

melting. The vertical profile of the TZ $\widetilde{\mathscr{A}}$ reveals a steady decrease of −0.18% $°C^{-1}$ to +4°C (Fig. 6). Inspection of the particle images from spiral 1 on 29 June and spiral 2 on 20 June indicated that evidence for melting was first detected at $T = +2.5°$ and 0°C, respectively. Representative particle plots from the 29 June spiral (M07, their Fig. 4) and the 20 June spiral (Fig. 8) illustrate the slow progression of melting to higher T, with particle shapes remaining predominately nonspherical. Ice was observed to T as high as +6.8°C in both spirals, with particles in the 20 June spiral never reaching melting completion before completely sublimating/evaporating and/or dropping below detectable concentrations.

Overall, the trends in $\log\widetilde{N_t}$ and $\log\widetilde{\mathbf{TWC}}$ support aggregation as an active process in the TZ, though the characteristic increase in $\widetilde{D_{mm}}$ with aggregation was not observed for most T. Considering the concurrent and rapid decrease in $\widetilde{\mathbf{RH}}$ with increasing T, sublimation likely countered any significant growth in particle size by aggregation.

The three TZ spirals profiles, executed across two MCSs, generally exhibited good agreement for each of the key variables (not shown). Despite this agreement—illustrated by the small spread of the TZ observations in Figs. 2–6—it is unknown how well those observations represent the TZ at large.

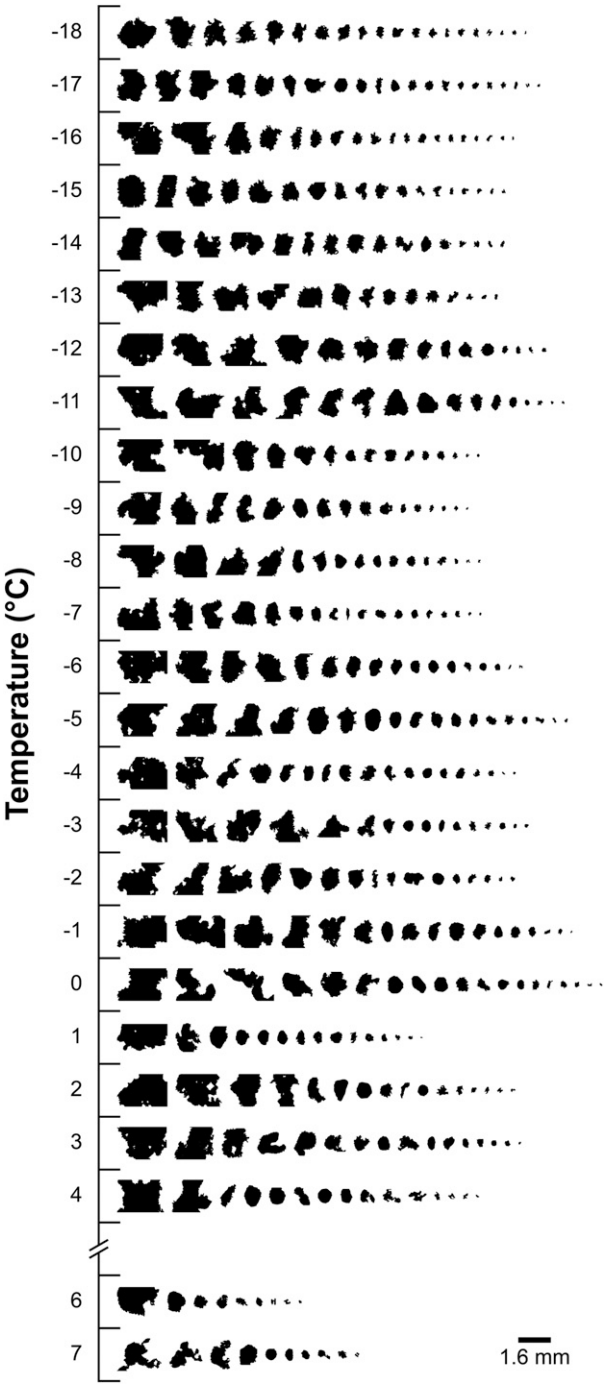

FIG. 8. Representative particle images observed by the CIP as a function of T (°C) within spiral 2 of the 20 Jun 2015 PECAN MCS.

An in-depth analysis of the three TZ spirals from PECAN and BAMEX was presented by S20, who showed that the environment of the TZ in the presence of the RIJ was considerably drier within and below the melting layer than observed within all other 20 June PECAN spirals apart from one in the AR. While falling

through the subsaturated region of the TZ, enhanced latent cooling at the surface of particles owing to sublimation and evaporation acts to significantly slow the progression of melting relative to observations in the ESR and AR. The latent cooling also contributes to the descent of the RIJ, with adiabatic warming during descent opposing the moistening imparted by sublimation and evaporation.

c. *Anvil region*

While AR observations were limited to only eight spirals, they were collected across five different MCSs. Thus, despite fewer spirals being performed than within the ESR, it is expected that these observations broadly define the characteristics of the AR. Most AR spirals were executed near cloud base, resulting in a limited number of brief excursions into areas of few cloud/precipitation particles (henceforth referred to as "clear air") within five spirals. These observations were retained in the final analyses and used in the computations of the averages in an effort to better characterize these regions. Excluding these observations predominately resulted in less negative fractional rates of change in $\log\widetilde{N}_t$ and $\log\widetilde{\mathbf{TWC}}$, with no significant impact on the conclusions of this study.

Compared to the TZ and ESR, the AR was associated with the greatest fractional rates of change in $\log\widetilde{N}_t$, and $\log\widetilde{\mathbf{TWC}}$ for $T \le 0°\text{C}$ (Figs. 3 and 4), with a $d\log\widetilde{N}_t/dT$ of $-28.9\%\ °\text{C}^{-1}$ and a $d\log\widetilde{\mathbf{TWC}}/dT$ of $-15.9\%\ °\text{C}^{-1}$ (Table 1). Over the same T, the AR had the lowest average $\widetilde{\mathbf{RH}}_i$ of the three MCS zones (Fig. 2), at 94.4% (Table 1), along with a $d\widetilde{\boldsymbol{D}}_{\text{mm}}/dT$ of $+132\,\mu\text{m}\,°\text{C}^{-1}$ (Fig. 5; Table 1), and a relatively constant $\widetilde{\mathscr{A}}$ (Fig. 6), exhibited by $d\widetilde{\mathscr{A}}/dT$ of $-0.01\%\ °\text{C}^{-1}$ (Table 1). While the sampling of different particle populations and occasionally clear air throughout each spiral affects a process-oriented interpretation, the reduction in $d\widetilde{\boldsymbol{D}}_{\text{mm}}/dT$ relative to that in the ESR and TZ, the virtually constant $\widetilde{\mathscr{A}}$, and predominately ice-subsaturated conditions combine to suggest that the effects of sublimation on aggregation were most prevalent in the subsaturated regions of the AR. This result is consistent with the column model study of G09, where latent cooling from sublimation was found to be the greatest in the subfreezing, subsaturated regions of the AR; possibly contributing to the descent of any rear-to-front flow.

Somewhat different localized trends were noted for locations immediately above the melting layer, approximately over $0° \ge T > -6°\text{C}$. There, $d\widetilde{\mathbf{RH}}_i/dT$ was $+4.3\%\ °\text{C}^{-1}$, $d\widetilde{\boldsymbol{D}}_{\text{mm}}/dT$ was far greater than for $T \le 0°\text{C}$, at $+441\,\mu\text{m}\,°\text{C}^{-1}$, $d\log\widetilde{N}_t/dT$ became more negative, at $-32.7\%\ °\text{C}^{-1}$, and $d\log\widetilde{\mathbf{TWC}}/dT$ increased to $-4.6\%\ °\text{C}^{-1}$. The percentage of CDP/FSSP N_t observations suggesting the presence of SLW gradually increased from 1% at −7°C to a maximum of 18% at −1°C. The sudden increase in $\widetilde{\mathbf{RH}}_i$, $\widetilde{\boldsymbol{D}}_{\text{mm}}$, and SLW coupled with a decrease in the rate of reduction of $\widetilde{\mathbf{TWC}}$ over $0° \ge T > -6°\text{C}$ suggests that the effects of sublimation were less important here, with aggregation and riming having more importance. These localized trends were reflected in the majority of the AR spirals, and may have resulted from a moistening of the environment associated with persistent sublimation and/or mesoscale ascent.

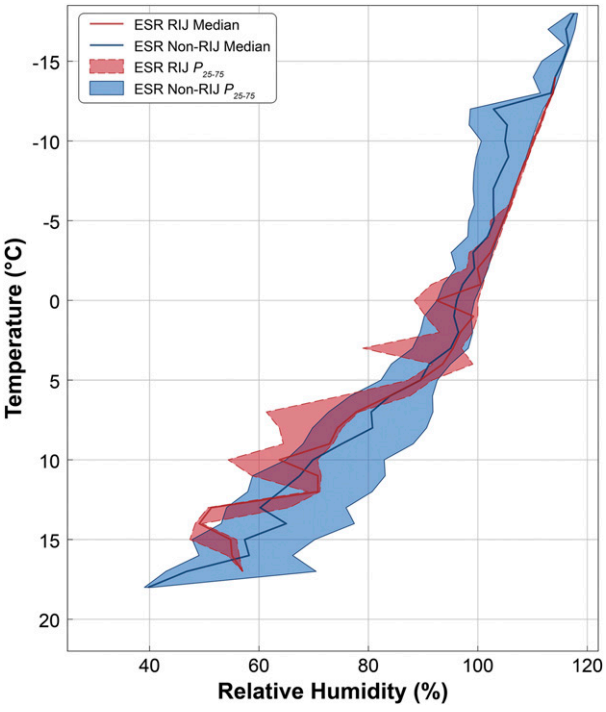

FIG. 9. Vertical profiles of $\widetilde{\mathbf{RH}}$ (%; red and blue solid lines) and the 25th–75th-percentile range of RH (%; red and blue shading) for the ESR RIJ and ESR non-RIJ classification sets as a function of T (°C). RH is with respect to ice for $T \le 0°\text{C}$ and with respect to liquid water for $T > 0°\text{C}$.

d. *Impacts of the RIJ within the ESR*

Airborne observations within or near the main axis of the RIJ of TS MCSs are exceedingly rare, with one BAMEX spiral profile in the TZ/notch, and three BAMEX spirals in the ESR the only such examples prior to PECAN. The PECAN dataset consists of two TZ and three ESR spiral profiles in or adjacent to the main axis of the RIJ, all sampled on 20 June. The three BAMEX and three PECAN ESR spirals that transected the RIJ (referred to as E-RIJ spirals) were compared to all other ESR spirals [referred to collectively as the non-RIJ spirals (E-NRIJ)] from BAMEX and PECAN to determine possible differences in the environment and particle populations owing to the presence of the RIJ.

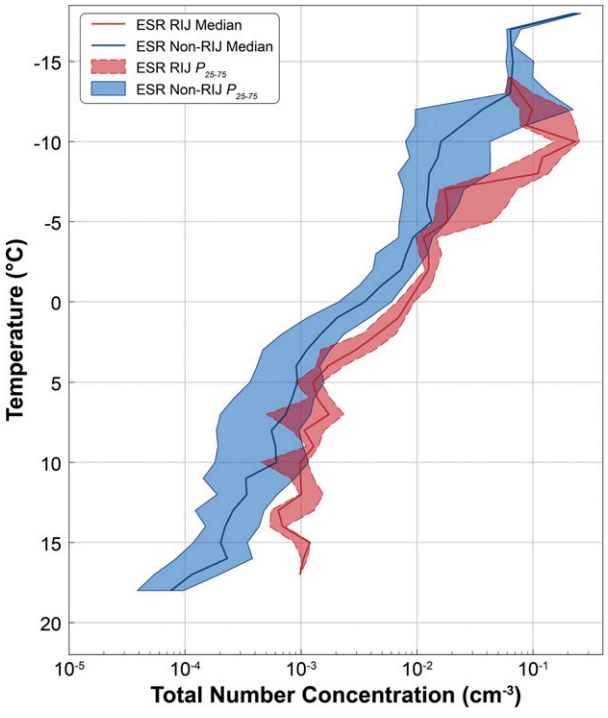

FIG. 10. As in Fig. 9, but for N_t (cm^{-3}).

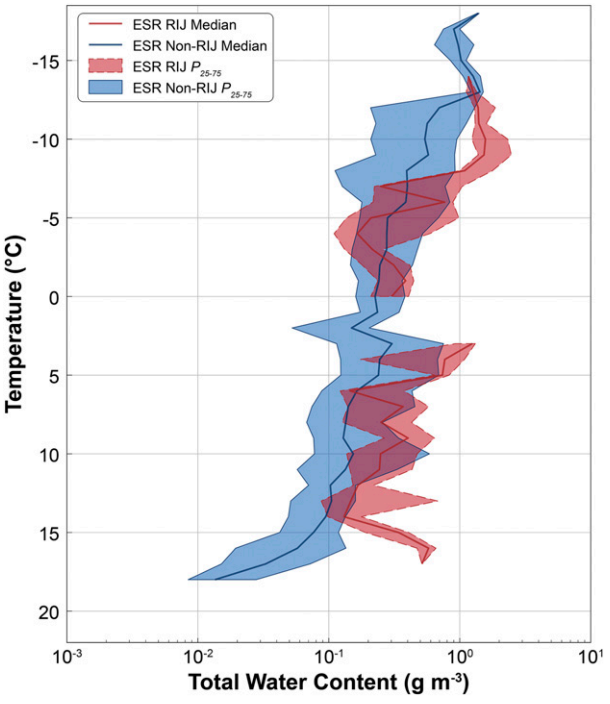

FIG. 11. As in Fig. 9, but for TWC (g m^{-3}).

Note that the BAMEX E-RIJ observations were limited to approximately $+7° \geq T \geq -7$°C.

The RIJ is expected to entrain dry air from the rear of the MCS into the ESR, which when coupled with adiabatic warming through any descent of the RIJ would locally decrease RH. Interestingly, $\widetilde{\mathbf{RH}}_i$ of the E-RIJ was greater than that of the E-NRIJ by ~1%–10% for $T < -1$°C (Fig. 9), and the average $\widetilde{\mathbf{RH}}_i$ of the two regions over all $T \leq 0$°C differed by only 0.1% (Table 1). The two regions also did not exhibit significant differences for $-1° \leq T \leq +6$°C, with several layers of drier conditions observed in the E-RIJ for $T > +6$°C.

For most T, the E-RIJ $\widetilde{N}_t$ exceeded that of the E-NRIJ by up to an order of magnitude, with nearly equal values only observed at $T = -14$°C (Fig. 10). Similarly, the E-RIJ $\widetilde{\mathbf{TWC}}$ was frequently greater than that of the E-NRIJ, though the spreads of TWC (Fig. 11) exhibited far more overlap than observed in the spreads of N_t. The $d\widetilde{N}_t/dT$ ($d\widetilde{\mathbf{TWC}}/dT$) was more negative in the E-RIJ than in the E-NRIJ, at −23.4% °C^{-1} (−16.4% °C^{-1}) and −20.7% °C^{-1} (−11.3% °C^{-1}), respectively (Table 1). These greater rates of decrease in $\widetilde{N}_t$ than $\widetilde{\mathbf{TWC}}$ with T for $T \leq 0$°C were present in both the E-RIJ and E-NRIJ, reflecting the same trends observed in the ESR as a whole and supporting aggregation as one of the primary active microphysical processes.

The greater rates of decrease in both $\widetilde{N}_t$ and $\widetilde{\mathbf{TWC}}$ with T within the E-RIJ compared to the E-NRIJ suggests sublimation was more actively limiting aggregation there relative to the E-NRIJ. The vertical profiles of D_{mm} (Fig. 12) and $\mathscr{A}$ (Fig. 13) support this apparent limitation on aggregation, as the E-RIJ had smaller values of $\widetilde{\boldsymbol{D}}_{\mathrm{mm}}$ and greater values of $\widetilde{\mathscr{A}}$ for most $T \leq 0$°C than observed in the E-NRIJ. Further, the characteristic increases in D_{mm} and decreases in $\mathscr{A}$ with increasing T expected with aggregation were less pronounced in the E-RIJ, with a $d\widetilde{\boldsymbol{D}}_{\mathrm{mm}}/dT$ ($d\widetilde{\mathscr{A}}/dT$) of +108 μm °C^{-1} (−0.16% °C^{-1}), compared to +150 μm °C^{-1} (−0.21% °C^{-1}) in the E-NRIJ (Table 1).

As discussed in section 3a, the percentage of ESR CDP/FSSP N_t observations suggesting the presence of SLW was greatest for $T > -5$°C. Considering the E-RIJ spirals only, the percentage of periods with SLW peaked for $-5° \leq T \leq -2$°C (Fig. 7), with a maximum of 45% at $T = -3$°C.

A limiting effect on aggregation by sublimation is indeed expected in the E-RIJ relative to the E-NRIJ, though the notably similar profiles of $\widetilde{\mathbf{RH}}_i$ complicate this interpretation. In addition, it remains unclear why the E-RIJ would be associated with higher total particle number and mass concentrations in addition to a higher incidence of SLW. The observations considered in this study were not suitable for tracking the evolution of individual particle populations, nor could the dynamics potentially affecting microphysical characteristics be resolved for each spiral. Factors that may have contributed

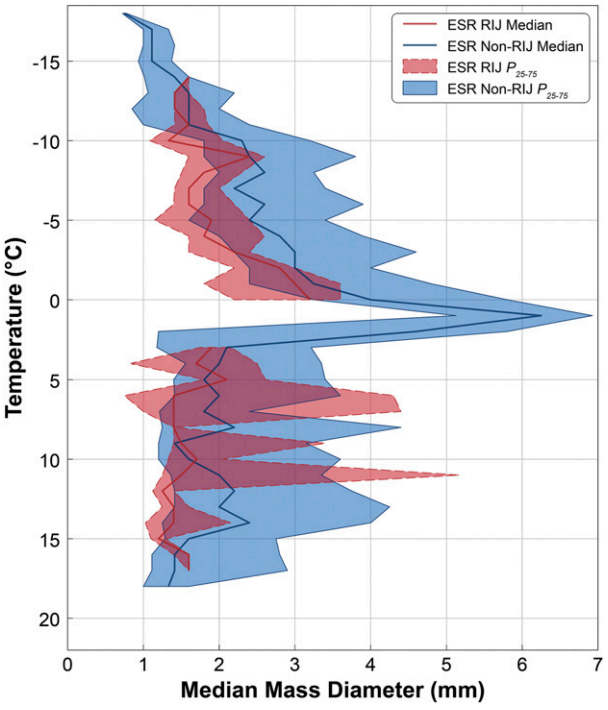

FIG. 12. As in Fig. 9, but for D_{mm} (mm).

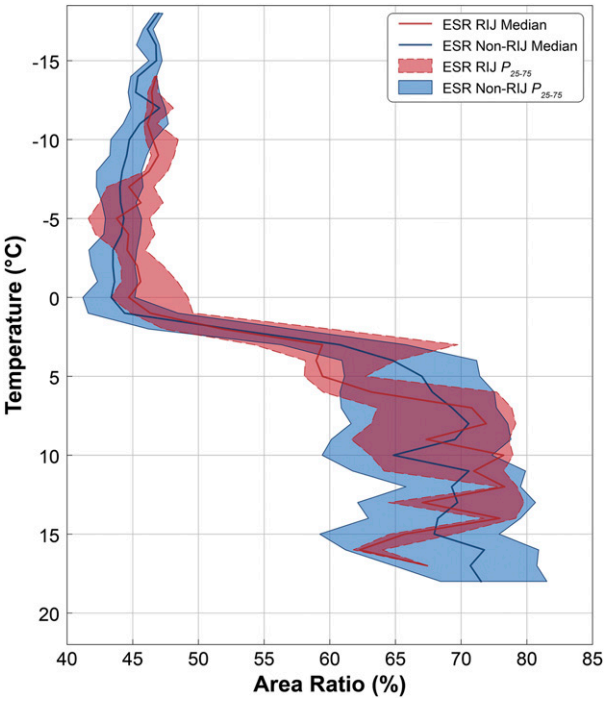

FIG. 13. As in Fig. 9, but for $\mathscr{A}$ (%).

to the observed relationships include the enhanced turbulence and horizontal convergence expected at the interface of the front-to-rear and rear-to-front flow regimes, as well as horizontal inhomogeneity and/or the sampling of different particle populations throughout each spiral.

e. *K-S test results*

To quantitatively evaluate the differences and similarities between MCS zones, the K-S test was applied to compare the TZ to the ESR, the TZ to the AR, the ESR to the AR, and the ESR non-RIJ spirals to the ESR RIJ spirals. The results of these tests for RH, N_t, TWC, D_{mm}, and $\mathscr{A}$ are given as a function of T in Fig. 14, where the p value significance threshold of 0.05 is indicated in each panel. A p value less than 0.05 suggests a probability of at least 95% that the two samples of some variable at a given ΔT were drawn from two separate distributions. The median p value from all ΔT in each zone/variable comparison is provided in Table 3, where bolded values indicate an overall rejection of the null hypothesis that the two samples were drawn from the same distribution.

The ESR exhibited statistically significant differences from both the TZ and AR when considering the median p values over all ΔT for each of the key variables, apart from the TZ versus ESR comparison of D_{mm}, which narrowly exceeded the significance threshold. When considering the vertical profiles of p values in the TZ versus ESR comparison, a higher incidence of threshold exceedance was observed for $T < -10$°C for RH_i, N_t, TWC, and D_{mm}. Meanwhile, the vertical profiles of p values for the ESR versus AR comparison did not reveal any such layers where differences between the two MCS zones were not consistently significant.

In the TZ versus AR comparison, the median p values for all key variables exceeded the significance threshold for $-5° \geq T \geq -15$°C, where a greater number of observations were obtained in both zones. The TZ versus AR comparison indicated that the differences observed in N_t, TWC, and D_{mm} were not statistically significant as a whole when considering the median p values over all T. Meanwhile, the TZ and AR distributions in RH and $\mathscr{A}$ exhibited greater and more frequent statistically significant differences than in N_t, TWC, and D_{mm}. All factors considered, particle population characteristics (N_t, TWC, and $\mathscr{A}$) within the TZ and AR are not statistically distinct, with less certainty in the similarity of particle morphology $\mathscr{A}$ and RH between the two regions, particularly for $T > -5$°C and $T < -15$°C.

Finally, the comparison of spirals within, to those removed from the RIJ in the ESR showed the two regions to be significantly different as a whole in terms of RH, N_t, and $\mathscr{A}$. The vertical profiles of p values indicate that the bulk of statistically significant differences were found above the melting layer, while median p values for $T > 0$°C easily exceeded the significance threshold for all

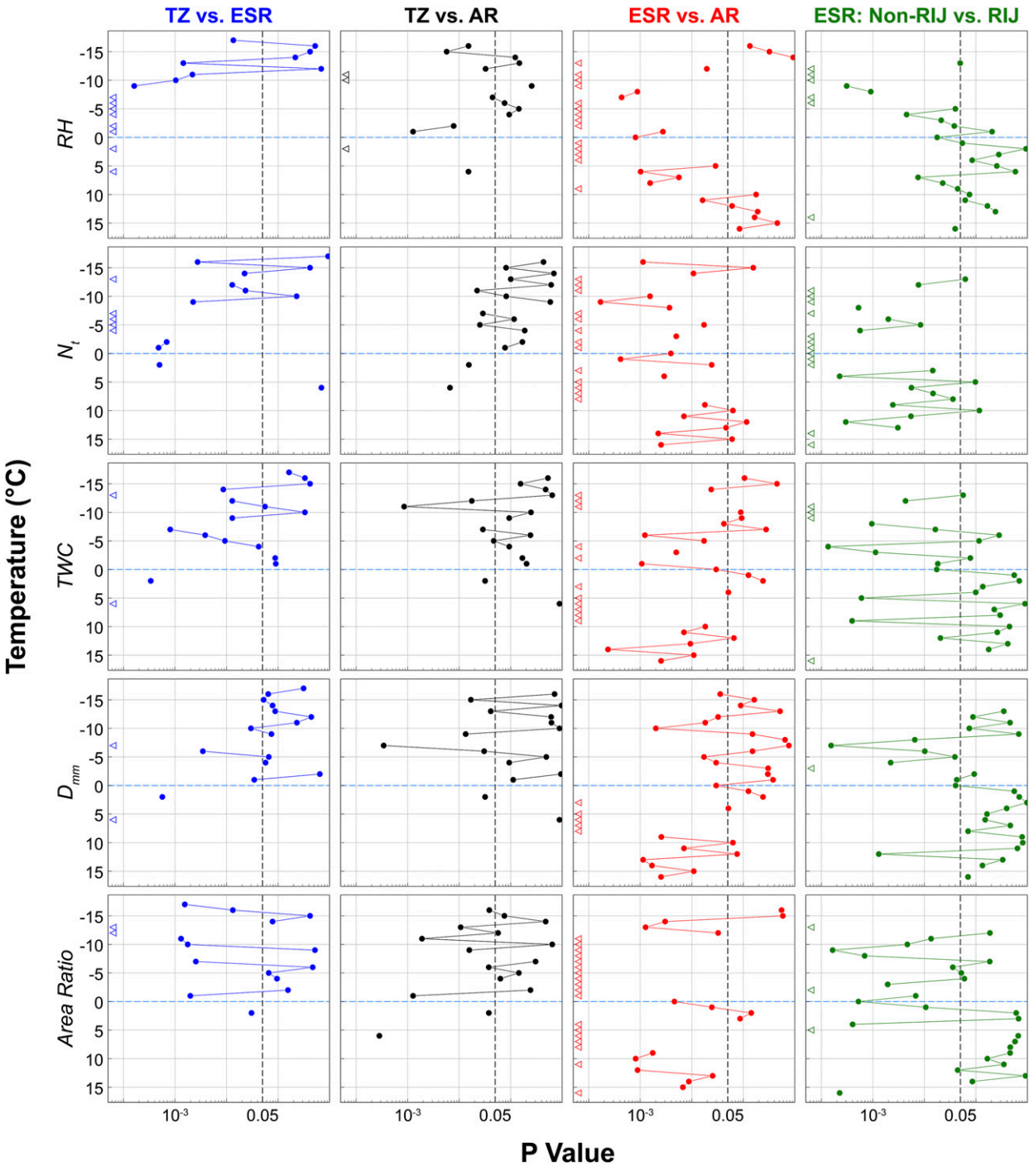

FIG. 14. Results of the K-S test for the (left to right) TZ vs ESR (blue traces), TZ vs AR (black traces), ESR vs AR (red traces), and the ESR RIJ vs ESR non-RIJ (green traces). The results of each comparison for (top to bottom) RH, N_t, TWC, D_{mm}, and $\mathscr{A}$ are given as a function of T (°C), where the 0.05 p value is indicated in each panel by a vertical dashed gray line. Triangles indicate p values less than 10^{-4} for a given interval of T. The $T = 0$°C level is denoted by the horizontal dashed blue line. RH is with respect to ice for $T \leq 0$°C and with respect to liquid water for $T > 0$°C.

TABLE 3. The median p value from all ΔT in each zone–variable comparison. Values are boldface where the median p value is less than 0.05, indicating an overall rejection of the null hypothesis that the two samples were drawn from the same distribution.

	TZ vs ESR	TZ vs AR	ESR vs AR	ESR: NRIJ vs RIJ
RH	$\mathbf{1.61 \times 10^{-4}}$	**0.024**	**0.001**	**0.040**
N_t	**0.002**	0.091	**0.002**	**0.001**
TWC	**0.013**	0.162	**0.007**	0.057
D_{mm}	0.064	0.301	**0.032**	0.134
$\mathscr{A}$	**0.013**	**0.048**	$\mathbf{2.44 \times 10^{-5}}$	**0.044**

variables except N_t. As such, the overall influence of the RIJ within the ESR was most significant for $T \leq 0$°C.

f. *Outlier spirals*

Most BAMEX and PECAN spirals exhibited ice particles of indeterminable habit. The ice particles observed within the PECAN postfrontal spiral profiles on 6 July were unique, with an abundance of relatively pristine particles including needles, columns, stellar dendrites, and spatial dendrites, along with aggregates distinctly composed of any of these (Fig. 15). Similar particles were also observed in a spiral behind the center of an MCV during the 24 May 2003 BAMEX mission.

The variation in the microphysical quantities with respect to T for $T < -5$°C within the postfrontal spirals was notably different than observed in the other spirals, with some similarity only to spiral 2 on 2 June 2003, and the 24 May 2003 spiral, both during BAMEX. Marked increases in both logN_t and logTWC with respect to increasing T were observed for $T < -5$°C in both postfrontal spirals and the 2 June BAMEX spiral (Figs. 16 and 17; Table 2), with a $d\log N_t/dT$ ($d$logTWC/dT) of +83% °C^{-1} (+70% °C^{-1}) in the first PECAN postfrontal spiral, +42% °C^{-1} (+15% °C^{-1}) in the second PECAN postfrontal spiral, and +67% °C^{-1} (+32% °C^{-1}) within the BAMEX spiral. Most other spirals discussed earlier exhibited decreases in logN_t and/or logTWC with increasing T above the melting layer, and any observed increases were of a smaller magnitude, over a smaller range of T, or both. Meanwhile, negligible trends were observed in logN_t and logTWC in the 24 May MCV spiral. Notably, the RH profiles for the PECAN postfrontal spirals and the BAMEX MCV spirals (not shown) were quite similar to those observed in the ESR. The 2 June BAMEX spiral occurred behind a bow echo, an environment common to many other PECAN and BAMEX spirals, with no evidence of pristine particles observed therein; both factors contributing to inclusion of the 2 June BAMEX spiral in the primary analysis set.

The PECAN postfrontal spirals and the BAMEX MCV spiral had significantly more CDP/FSSP N_t observations

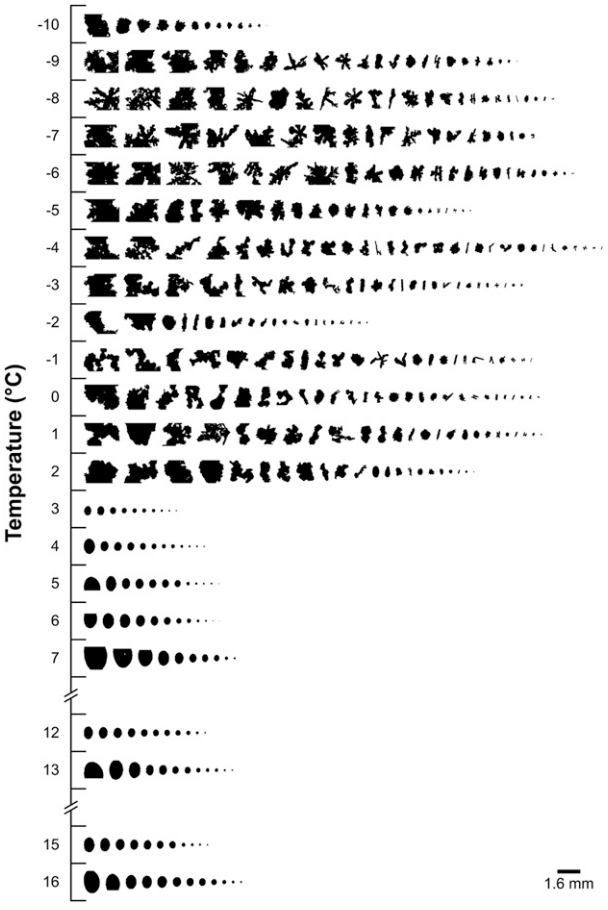

FIG. 15. Representative particle images observed by the CIP as a function of T (°C) within spiral 2 of the 6 Jul 2015 PECAN MCS.

suggesting the presence of SLW than seen in any of the other spirals; predominately for $-10° \leq T < -6$°C within the BAMEX MCV spiral, and for nearly all $T \leq 0$°C within the PECAN postfrontal spirals (Fig. 7).

Further study is warranted to determine what processes may have been common among these spirals that contributed to their shared characteristics. The increases in logN_t and logTWC with increasing T combined with the presence of pristine ice particles and a high incidence of SLW within the postfrontal spirals suggests that a gradual uplift mechanism of some sort may have been present to the rear of the frontal squall line that contributed to new particle formation and growth. Such a mechanism was absent, or at least less prominent, within the MCS environments of the other spirals.

4. Discussion and conclusions

This study provided an analysis of airborne in situ observations obtained within 52 spiral profiles of the NOAA P-3 during the 2003 BAMEX and 2015 PECAN

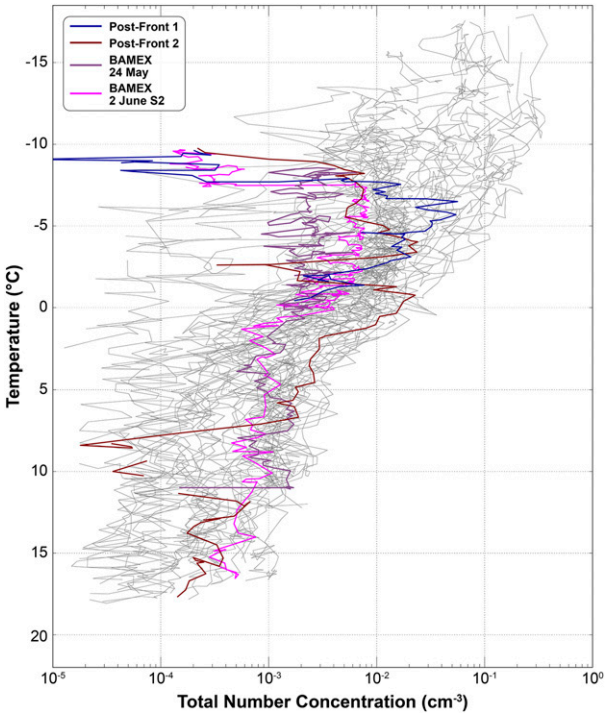

FIG. 16. Vertical profiles of N_t (cm^{-3}) as a function of T (°C) from the two PECAN postfrontal spirals (dark blue and dark red lines), the 24 May 2003 BAMEX spiral (dark purple line), and spiral 2 from the 2 Jun 2003 BAMEX MCS (magenta line). Profiles from each of the other BAMEX and PECAN spirals in the primary analysis set are underlaid for reference (thin dark gray lines).

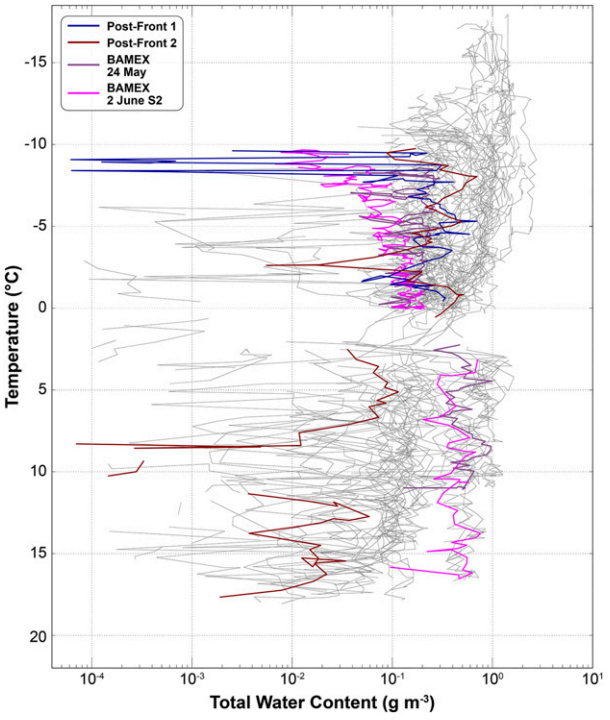

FIG. 17. As in Fig. 16, but for TWC ($g\ m^{-3}$).

field campaigns to characterize the vertical variability of thermodynamic and microphysical properties and inferred processes across MCS zones. Comparisons were made for the three MCS zones, namely, the TZ, ESR, and AR, with separate consideration of two spirals that sampled the region immediately behind a frontal squall line, which exhibited notably different microphysical characteristics than seen in all but one BAMEX spiral and all PECAN MCS spirals. Furthermore, characteristics of spirals within the ESR both within and removed from the RIJ were compared to identify potential changes attributable to the presence of the RIJ. The primary findings of the combined spiral analysis were as follows:

1) Aggregation was the dominant process affecting the microphysical characteristics within the ESR for $T \leq 0$°C, as evidenced by the greatest rate of decrease of $\widetilde{\mathscr{A}}$, increases in $\widetilde{\boldsymbol{D}_{\rm mm}}$, and greater rates of decrease of $\widetilde{\boldsymbol{N}_t}$ than $\widetilde{\mathbf{TWC}}$ on average compared to spirals in other regions, all relative to increasing T. Minimal influence by sublimation is expected given $\widetilde{\mathbf{RH}_i}$ values predominantly near or exceeding ice saturation.
2) Sublimation cooling at the surface of ice particles owing to subsaturation above, within, and below the melting layer within a subset of seven ESR spirals allowed for a delay in the onset of melting to +2.5°C on average. A continued increase in $D_{\rm mm}$ and enhanced decrease in $\mathscr{A}$ between $T = 0$°C and melting onset indicate that aggregation persisted and potentially became more effective through this layer.
3) The TZ was the driest of the MCS zones, with subsaturated conditions present on average for $T > -9$°C. Despite a layer of apparent particle growth between −13°C and −8°C, where $d\widetilde{\boldsymbol{D}_{\rm mm}}/dT$ approached $+1\ {\rm mm\,°C^{-1}}$, evidence of aggregation for $T \leq 0$°C was primarily limited to a greater rate of decrease in $\widetilde{\boldsymbol{N}_t}$ than $\widetilde{\mathbf{TWC}}$. An absence of trends in $\widetilde{\boldsymbol{D}_{\rm mm}}$ otherwise, together with a rapid and persistent decrease in $\widetilde{\mathbf{RH}_i}$ indicates that sublimation actively limits the effectiveness of aggregation in the TZ.
4) The AR had the lowest average median values of $\mathbf{RH}_i$, $\boldsymbol{N}_t$, and $\mathbf{TWC}$ for $T \leq 0$°C compared to the other spiral locations. Compared to the TZ and ESR, the greatest fractional rates of change in $\log\widetilde{\boldsymbol{N}_t}$ and $\log\widetilde{\mathbf{TWC}}$ for $T \leq 0$°C were observed in the AR, along with a negligible decreasing trend in $\widetilde{\mathscr{A}}$ and the largest average $\widetilde{\mathscr{A}}$ for the same T. Taken together, these results indicate that the impacts of sublimation on aggregation were most prevalent in the subfreezing and subsaturated regions of the AR.
5) Comparison between ESR spirals within and removed from the RIJ revealed that spirals in the

vicinity of the RIJ had greater fractional rates of decrease in both total particle number and mass concentrations with increasing T, with lower values of $\widetilde{D}_{mm}$ and greater values of $\widetilde{\mathscr{A}}$ for most $T \leq 0°C$. These results, together with slower rates of increase in $\widetilde{D}_{mm}$ and decrease in $\widetilde{\mathscr{A}}$ within the spirals conducted in the vicinity of the RIJ indicate that while aggregation was an active process in both the RIJ and non-RIJ spirals, sublimation and/or effects associated with the dynamics of the RIJ seemingly played a larger role in modifying the particle population in the presence of the RIJ.

6) The ESR had the most statistically significant differences from the other regions when considering comparisons of RH, N_t, TWC, D_{mm}, and $\mathscr{A}$. Meanwhile, observations within the TZ and AR were statistically indistinct from one another for most $T < -5°C$, a finding that may be at least partially skewed by limited sample sizes in these two regions.
7) Three spirals had significantly different characteristics than generally observed in all of the other BAMEX and PECAN MCS spirals. These outlier spirals exhibited a high incidence of pristine ice particles, including aggregates that were composed of identifiable component habits. Particle number and mass concentrations were observed to *increase* with increasing T for $T < -5°C$ in two of these spirals, immediately behind a frontal squall line, in direct contrast to the decreases observed in these quantities on average in most other spirals.

In summary, aggregation was ubiquitous within all MCS zones, though the effectiveness of this process was modified to varying degrees depending on the ambient subsaturation. The ESR was associated with the greatest average RH, and exhibited the least impacts of sublimation on microphysical characteristics relative to the TZ and AR.

The limiting effects of sublimation on aggregation were most prevalent in the subfreezing, subsaturated regions of the AR, consistent with the column model study of G09, where latent cooling from sublimation was found to be the greatest. Similar effects were observed in the TZ in this study, where all three TZ spirals were executed within the rear inflow notch of the MCS. As discussed by G09 and S20, the RIJ entrains dry air from the rear of the MCS, which when coupled with adiabatic warming associated with the descent of the RIJ, produces the deficit in RH observed relative to the ESR and AR for $T > -4°C$. Meanwhile, regions in the vicinity of the RIJ within the ESR are generally associated with observable modification of aggregation via enhanced sublimation, leading to less particle growth and lower particle number and mass concentrations.

This study yielded analyses of the largest and most diverse set of in situ microphysical observations within midlatitude MCSs to date, with three spiral profiles in the TZ across two MCSs, eight spirals in the AR across five MCSs, and 39 spirals in the ESR across 13 MCSs. Despite the relative enormity of this dataset, there remain uncertainties as to the overall representativeness of the analyses for regions with few spiral profiles, and/or regions dominated by observations within a small number of parent MCSs. Additionally, there is still uncertainty concerning the sensitivity of microphysical characteristics and processes to the structure and intensity of, and horizontal distance from, the convective line. To improve the representativeness of these analyses and reduce statistical uncertainty, future field operations should focus on gathering observations within more MCSs and in each MCS region (especially the TZ and AR), ideally terminating closer to cloud top. Similar studies using remote sensing retrievals, evaluated against collocated in situ observations, could increase the spatial and temporal sampling of such phenomena.

Acknowledgments. This study was funded by the National Science Foundation under Grants AGS-1359098, AGS-1842094, and AGS-1841966, with additional support provided by the NSSL Director's Discretionary Research Fund. We thank the NOAA P-3 flight crew for acquiring the PECAN dataset. Conrad Ziegler and David Jorgensen of the National Severe Storms Laboratory (NSSL) are acknowledged for their efforts in obtaining flight hour support for the P-3 service during PECAN. Some of the computing for this project was performed at the University of Oklahoma (OU) Supercomputing Center for Education and Research (OSCER). We also acknowledge Troy Zaremba and Brittany Welsh, who manually identified the majority of the representative particle images for the PECAN spirals, and Kimberly L. Elmore, who provided guidance pertaining to the implementation of the two-sample K-S test. We appreciate the constructive comments of Matthew Parker and two other anonymous reviewers.

APPENDIX

Overviews of BAMEX and PECAN Missions

Overviews of each BAMEX and PECAN mission included in the present study are given in this appendix. Animations illustrating the P-3 flight track atop WSR-88D composite reflectivity (at 1 km AGL) for each of the PECAN missions are provided in the online supplement for this paper as Animations A, B, C, D, and E,

corresponding to the PECAN cases of 17 June, 20 June, 1 July, 6 July, and 9 July 2015, respectively.

a. 17 June 2015: PECAN IOP11

IOP11, on 17 June 2015 in northwestern and central Nebraska, was the first P-3 mission of PECAN. Convection initiated at approximately 2130 UTC 16 June along a prefrontal trough, with storms exhibiting supercellular structure by 0000 UTC 17 June. The P-3 approached the region at 0145 UTC (Fig. A1a), at which time the supercells exhibited a tendency toward upscale organization, while a separate and disorganized area of stratiform precipitation approached from the Nebraska Panhandle. Between 0356 and 0526 UTC, the P-3 conducted the first three spirals (Figs. A1b–d), while the two original supercells evolved into a TS MCS. During spirals 1–3, the targeted areas of the ESR rapidly eroded, so that the observations were predominantly below the anvil cloud base, which was located at approximately 6.6 km MSL based on TDR reflectivity. Spiral 2 contained sufficient in-cloud observations for inclusion in this study, though the majority of spirals 1 and 3 occurred in clear air and were excluded. Between 0539 and 0649 UTC, the P-3 conducted spirals 4, 5, and 6 within the trailing edge of the ESR, during which the MCS did not exhibit significant changes in low-level reflectivity structure (Figs. A1e–g), maintaining a well-defined leading convective line, TZ, and ESR. The seventh, and final, spiral sampled the leading edge of the ESR 37 km from the convective line (Fig. A1h). Hitchcock et al. (2019) provided additional details concerning this MCS and the evolution of its pre and postconvective environment, while Kumjian et al. (2018) explored hail detection and sizing using dual-frequency, dual-polarization radar observations in the early stages of this system.

b. 20 June 2015: PECAN UFO4

The 20 June 2015 UFO4 MCS began as a group of supercells in southeastern Montana and northeastern Wyoming, which initiated ahead of a weak cold front at approximately 2100 UTC 19 June. Intersection of a low-level jet with a strengthening east–west baroclinic zone across northern Wyoming into southwestern South Dakota assisted in the eventual upscale growth of the supercells into a TS MCS by 0400 UTC 20 June. The P-3 executed spirals 1 and 2 behind a developing bow echo between 0456 and 0513 UTC. These spirals occurred within the TZ and were collocated with the rear inflow notch. Though the rear inflow notch is most commonly associated with a weakened precipitation echo to the rear of the ESR (e.g., Smull and Houze 1985), it may also refer to the "weak-echo channel" that extends through the ESR toward the convective line (e.g., Przybylinski 1995; Alfonso and Naranjo 1996; Weisman 2001). Spiral 1 was shallower (1.4 km) than most spirals, with observations confined to $T \leq -9.3°C$. Spiral 2 fully transected the RIJ, with a peak in ground-relative wind speeds of $37\,m\,s^{-1}$ just below the melting layer. Spiral 3 occurred in the AR to the north of the RIJ axis between 0521 and 0537 UTC. The P-3 returned southeast and executed spirals 4 and 5 consecutively in the trailing half of the ESR between 0547 and 0622 UTC, coincident once again with the RIJ axis. Spiral 6 was conducted between 0638 and 0647 UTC in the expansive stratiform region to the north of spirals 4 and 5, and was the sole ESR spiral removed from the RIJ axis within this MCS. A final spiral was executed between 0709 and 0746 UTC at the leading edge of the ESR, where flight-level wind speeds of $43\,m\,s^{-1}$ were recorded, associated with the RIJ. At this time, the convective line had a very well-defined bowing structure complete with bookend vortices. A more detailed overview and analysis of this MCS is provided by S20.

c. 1 July 2015: PECAN IOP17

The 1 July 2015 IOP17 MCS was highly disorganized, most characteristic of the nonlinear MCS archetype. A swath of predominantly stratiform precipitation began filling in toward the south along the Nebraska–Iowa border at approximately 1200 UTC 30 June, associated with persistent southerly flow intersecting an east–west baroclinic zone near the northern border of Missouri. This region of precipitation persisted through the daytime hours, and gradually moved southward with occasional periods of embedded convection. The P-3 took off at approximately 0400 UTC 1 July, at which time a weakly coherent nonlinear MCS had formed, with a broken line of convection extending from east-central Nebraska, through southwest Iowa, and into north-central Missouri (Fig. A2a). The P-3 arrived onsite shortly before 0500 UTC, when a marginal convective structure was beginning to dissipate (Fig. A2b). Between 0604 and 0620 UTC the P-3 conducted a spiral descent through the ESR (Fig. A2c). After passing through the melting layer and reaching the bottom of the descent, the P-3 crew reported that the deicing system was nonfunctional, which necessitated the remainder of the flight remain at $T > 0°C$, precluding any additional spiral profiles. More details concerning the characteristics of this system are given by Lin et al. (2019), along with an examination of the interaction between MCS inflow and outflow using airborne observations from the compact Raman lidar.

d. 6 July 2015: PECAN IOP20

The observations collected during the 6 July 2015 IOP20 MCS are the most complete and diversified of PECAN, both in terms of the assets deployed and their

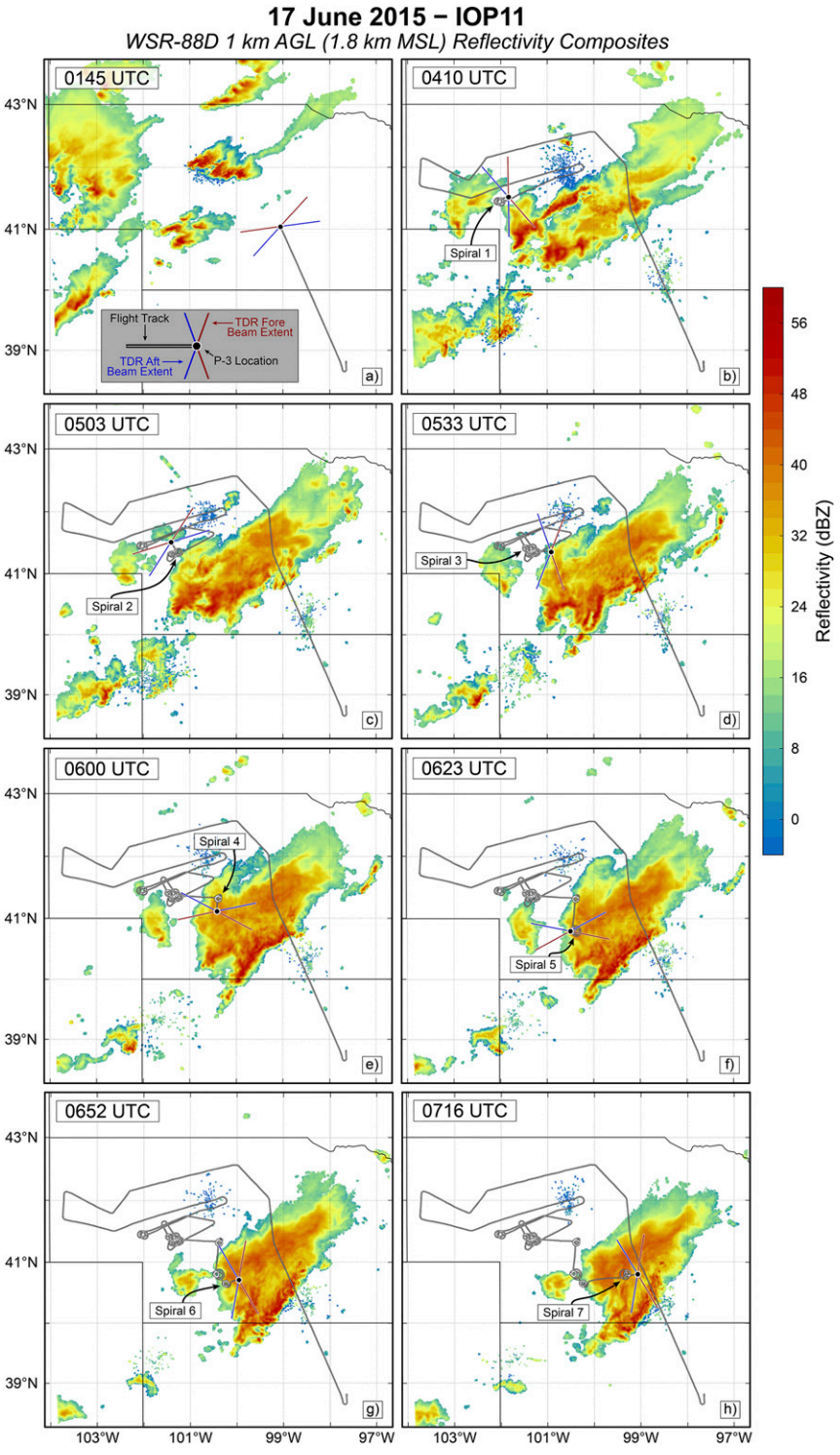

FIG. A1. Radar reflectivity composites at 1 km AGL (1.8 km MSL) composed of WSR-88D observations of the 17 Jun 2015 IOP11 MCS. Key periods discussed in the text are shown between 0145 and 0716 UTC, with the flight track (white line, black edge) and location of the P-3 at indicated times (black dot, white edge) shown along with the location and maximum range of the fore and aft beams of the TDR (red and blue lines, respectively).

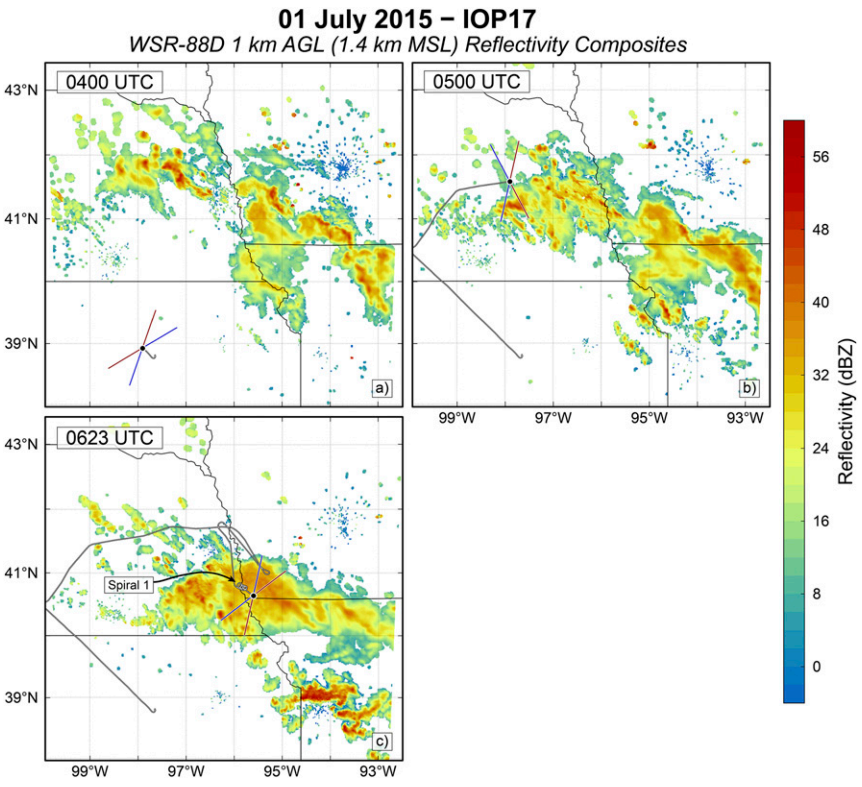

FIG. A2. As in Fig. A1, but for the 1 Jul 2015 IOP17 MCS. Key periods discussed in the text are shown between 0400 and 0623 UTC.

locations relative to the system. An overview of this MCS and its evolution is provided by Bodine and Rasmussen (2017), and Flournoy and Coniglio (2019) assimilated observations of this system into a simulation to explore the development of an observed tornadic mesovortex. A brief synopsis is provided here, with an emphasis on how the storm evolution relates to the timing and location of the P-3 spiral profiles.

The 6 July convective system consisted of an initially separate and distinct MCS that grew upscale from convection initiated by focused ascent associated with a 500 hPa shortwave trough over eastern Montana and Wyoming around 2300 UTC 5 July. In addition, convection initiated in northeast South Dakota around 0000 UTC 6 July along a convergent boundary between a cold front and the low-level jet, with convection expanding along the front to the west-southwest and east-northeast with time. Around 0350 UTC, the convective line of the southern MCS intersected the southern tip of the frontal squall line, and stratiform precipitation associated with both the MCS and preexisting convection in northern South Dakota began to fill in behind the front and to the north of the MCS (Fig. A3a). The P-3 executed the first two spirals of the mission between 0319 and 0345 UTC just behind the frontal squall line to the northeast of the MCS/squall line intersection (Fig. A3a). The ascent of spiral 1 began at approximately 4.5 km MSL with observations constrained to $T < 0$°C. The frontal squall line lacked a well-defined ESR at this time, and little to no precipitation reached the surface beneath the spirals. Although spirals 1 and 2 were associated with similar reflectivity structures as might be found in a formative TZ, the differences in kinematic and dynamic structure between a leading-line–trailing-stratiform MCS and a frontal squall line warranted the aforementioned postfrontal classification.

Following spirals 1 and 2, the P-3 proceeded southwest to the stratiform region immediately north of the MCS–squall line intersection and began the third spiral at 0423 UTC in the ESR (Fig. A3b), by which time a secondary line of convection had formed ahead of the squall line. Spiral 3 was immediately followed by a spiral descent in the same location, concluding at 0453 UTC (Fig. A3c), when the convective line of the southern MCS appeared to be weakening and the frontal squall line had converged with the secondary line ahead of it. The P-3 executed spirals 5 and 6 in the ESR between 0540 and 0613 UTC (Figs. A3d,e), prior to which the MCS and squall line had merged into a single convective system. Spirals 7 and 8 were executed within the ESR

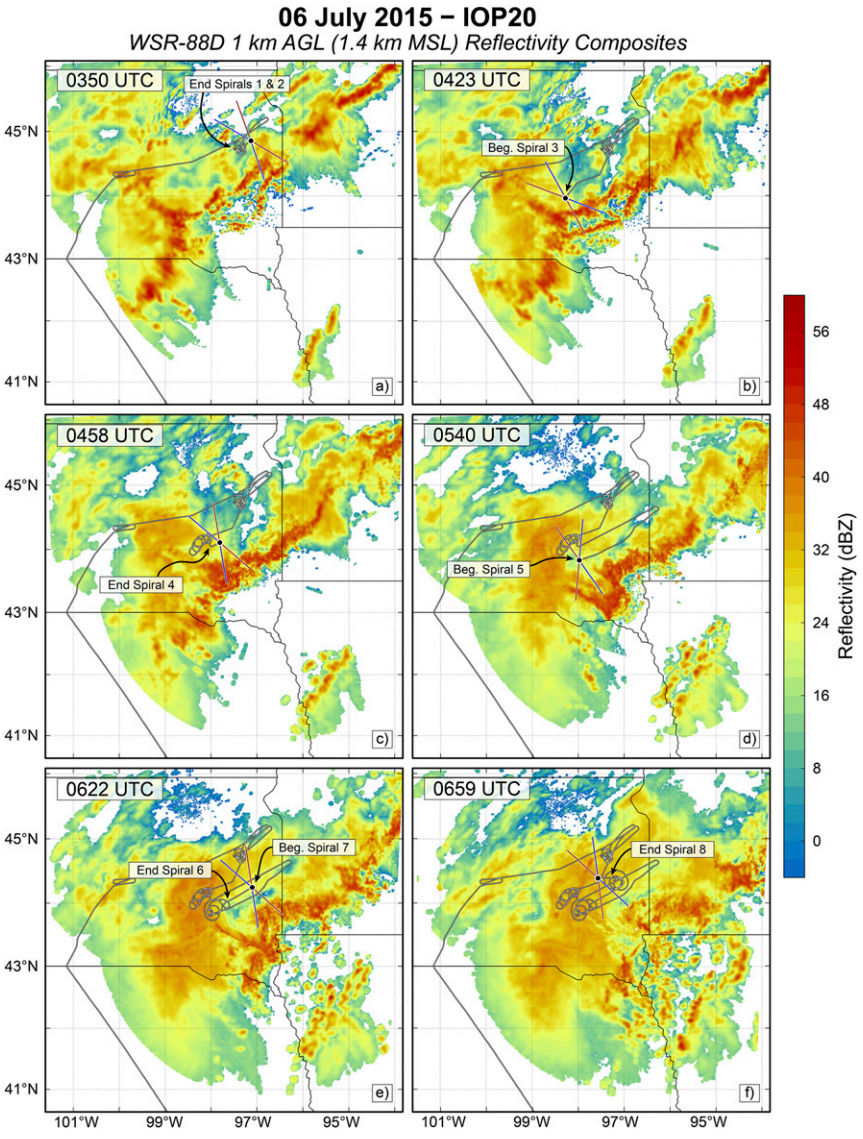

FIG. A3. As in Fig. A1, but for the 6 Jul 2015 IOP20 MCS. Key periods discussed in the text are shown between 0350 and 0659 UTC.

behind the squall line between 0622 and 0654 UTC (Figs. A3e,f).

The 6 July convective system yielded two postfrontal spiral profiles to the northeast of where an MCS intersected a frontal squall line, four spirals in the mature ESR formed by the merger of the two systems, with an additional two spirals in the mature ESR trailing the frontal squall line.

e. 9 July 2015: PECAN IOP21

At approximately 2000 UTC 8 July 2015 a group of convective cells initiated and organized in far northeastern New Mexico, east of a 500-hPa trough aloft. The formative MCS propagated to the southeast into the center of the Texas Panhandle by 0125 UTC 9 July, at which time the MCS consisted primarily of a leading convective line with hints of a stratiform region forming along its northeastern edge. The P-3 sampled along the northwestern flank of the convective line before executing the first two spirals between 0227 and 0253 UTC, within and beneath the periphery AR and behind the convective line (Fig. A4a). The P-3 shifted to the southwest to perform spirals 3 and 4 between 0257 and 0322 UTC in a region still best characterized as the AR (Fig. A4b). Between 0125 and 0325 UTC, the MCS developed a bow and arrow structure (e.g., Keene and Schumacher 2013) with an ESR primarily to the northeast, parallel to the convective line, and a narrow,

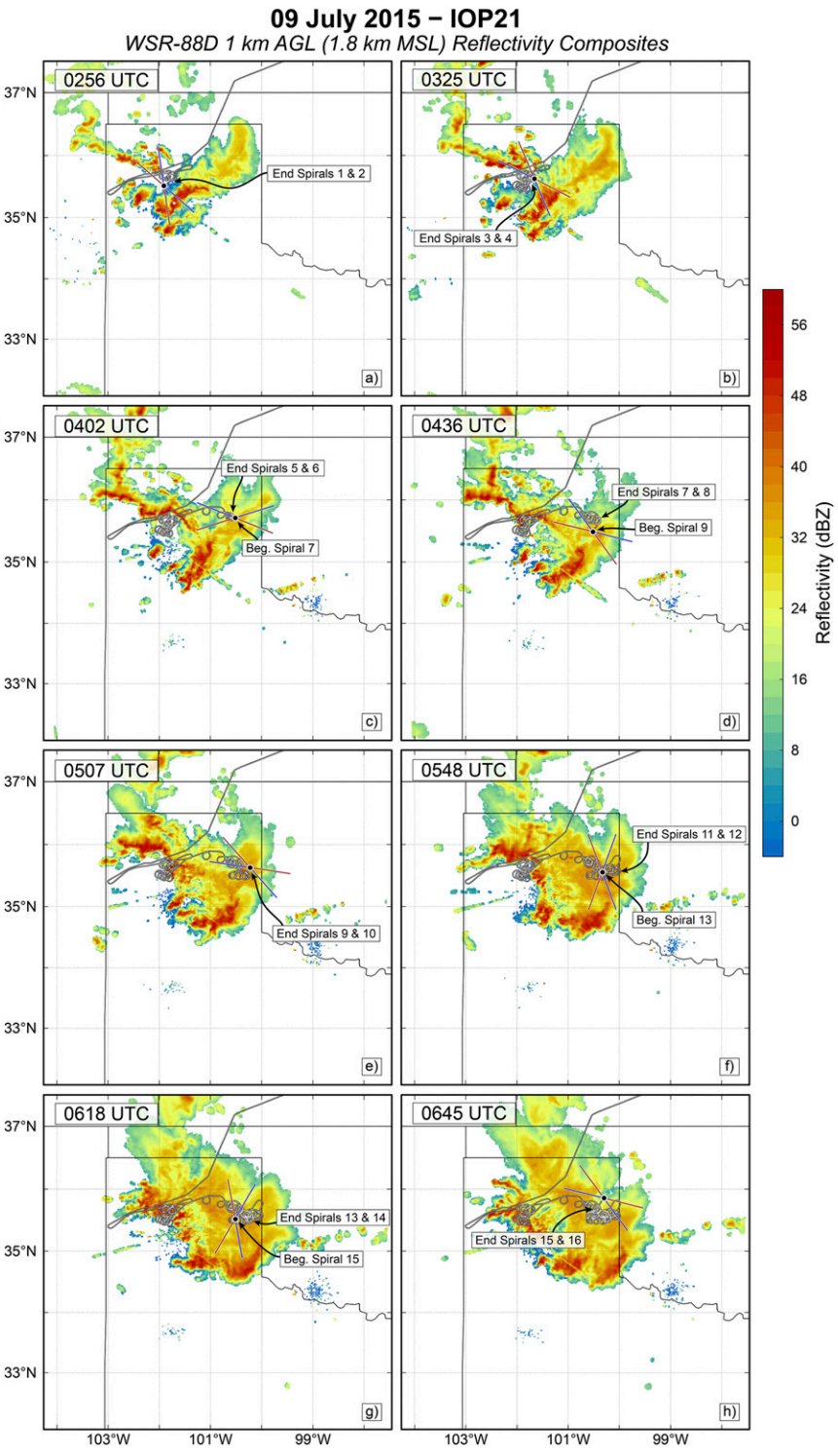

FIG. A4. As in Fig. A1, but for the 9 Jul 2015 IOP21 MCS. Key periods discussed in the text are shown between 0256 and 0645 UTC.

quasi-stationary line of convection extending to the west-northwest, nearly orthogonal to the primary convective line.

The P-3 shifted northeast into the parallel ESR after spiral 4 and proceeded to consecutively execute spirals 5–8 between 0332 and 0429 UTC (Figs. A4c,d). Stratiform precipitation was increasing in coverage trailing the convective line by 0436 UTC, prompting a change in system classification to leading-line–trailing-stratiform for the remaining spirals, all of which sampled the ESR. Spirals 9 and 10 commenced between 0436 and 0503 UTC, during which time the main convective line had shifted from a south-southwest/north-northeast orientation to a nearly east–west orientation (Fig. A4e). The remaining six spirals were conducted nearly back-to-back between 0517 and 0641 UTC (Figs. A4f–h), with spirals 6–16 all occurring within a circular region less than 40 km in diameter. During these eleven spirals, the MCS and convective line remained nearly stationary, while very slowing expanding to the east into Oklahoma, and maintaining a western border near Amarillo.

The 9 July IOP21 MCS in the panhandle of Texas yielded 16 spiral profiles, half of which sampled the system when it had a parallel stratiform structure, and the final half when the MCS had transitioned to a TS structure. Four spirals were executed within and beneath the AR behind a developing bow echo, while the remaining 12 spirals were within a focused region of a well-defined and nearly stationary ESR. This MCS accounted for 31% of all ESR spirals across both BAMEX and PECAN, and 50% of all AR spirals.

f. 24 May 2003: BAMEX IOP1

On 24 May 2003, the P-3 targeted the stratiform rain region to the north of an MCV circulation center in northern Arkansas, where a single spiral was executed between 2150 and 2232 UTC. The MCV was associated with weak convective structures embedded within a broad area of stratiform precipitation. Further details concerning this event are given by Davis and Trier (2007) and James and Johnson (2010).

g. 31 May 2003: BAMEX IOP3

After 0100 UTC 31 May 2003, a line of supercells focused along a strong cold front moved through northern and central Illinois, growing upscale into a well-defined leading-stratiform MCS by 0200 UTC. The system persisted into and through Indiana, developing a small trailing ESR in addition to the much larger leading ESR by 0400 UTC. Between 0432 and 0527 UTC, the P-3 executed a single spiral in the trailing ESR. Additional details of the 31 May MCS are given by Wheatley et al. (2006) and Storm et al. (2007).

h. 2 June 2003: BAMEX IOP4

Convective activity tracked eastward through Arkansas through the morning on 2 June 2003, with periods of weakly coherent squall line organization. By 1700 UTC, a small convective line with no associated stratiform region was located in southwest Arkansas, with a separate, broad area of stratiform precipitation trailing a moderately organized convective line to the north of Little Rock. The P-3 executed spiral 1 in this ESR between 1755 and 1818 UTC. Between 1830 and 2100 UTC, the convective line south of Little Rock developed into a well-defined TS MCS as it tracked toward the Mississippi border. The P-3 conducted a final spiral in the ESR of this MCS between 2110 and 2203 UTC. Further overview and analysis of this system is provided by Wakimoto et al. (2015).

i. 10 June 2003: BAMEX IOP7A

Between 0100 and 0300 UTC 10 June 2003, two discrete supercells in northeastern and east-central Nebraska rapidly evolved into two small-scale bow echoes. These bow echoes merged into a single, large bowing MCS with trailing stratiform precipitation by 0600 UTC as the system propagated into northwestern Missouri. The P-3 executed spiral 1 in the ESR between 0717 and 0740 UTC, and transected a very strong descending RIJ with observed flight-level wind speeds of 39 $m\,s^{-1}$ (SM09). The system continued to propagate south-southeastward through Missouri through 1000 UTC, with a final spiral in the mature ESR between 0942 and 1015 UTC. Further details concerning this MCS are given by Wheatley et al. (2006) and Melhauser and Zhang (2012).

j. 21 June 2003: BAMEX IOP9

Prior to 0000 UTC 21 June 2003, disorganized convection was scattered across northeast Colorado. By 0100 UTC, an MCS began to rapidly evolve, developing a southwest–northeast-oriented convective line, with a broad region of asymmetric trailing stratiform precipitation to the northwest. The system began to weaken while over west-central Nebraska around 0430 UTC, at which time the P-3 was to the rear of the ESR and executed a single spiral in the AR between 0454 and 0506 UTC.

k. 26 June 2003: BAMEX IOP13

On 25 June 2003, a strong cold front served as the nexus for convective initiation and subsequent organization into a TS MCS by 0000 UTC 26 June, with a southwest–northeast-oriented convective line draped across central Illinois. The P-3 conducted a single spiral

in the ESR behind a weakening bowing segment between 0128 and 0202 UTC.

l. 29 June 2003: BAMEX IOP14

The 29 June 2003 MCS evolved along and ahead of a weak frontal boundary, with convection organizing into a coherent east–west line in northern Kansas by 0500 UTC. The first P-3 spiral was executed between 0526 and 0538 UTC near the ESR–TZ boundary, within a weak-echo channel associated with the rear inflow notch. The convective line began to weaken and dissipate by 0700 UTC, while a broad ESR persisted. The P-3 conducted a final spiral within the remnant ESR between 0729 and 0741 UTC. An overview of this MCS, complete with an analysis of the RIJ development is provided by Grim et al. (2009b).

m. 3 July 2003: BAMEX IOP16

Around 0100 UTC 3 July 2003, a roughly east–west-oriented convective line with trailing stratiform precipitation formed in central Minnesota, with initiation supported by outflow boundaries from earlier convection to the northeast. The MCS moved toward the south-southwest over the next few hours, developing numerous bowing segments and a few confirmed tornadoes. The P-3 executed a single spiral in the mature ESR between 0518 and 0529 UTC.

n. 5 July 2003: BAMEX IOP17

Convection initiated in northeastern Illinois around 2000 UTC 4 July 2003, focused along a remnant outflow boundary. A TS MCS rapidly organized from this convection by 2200 UTC, and moved southeastward into northern Indiana. By 0000 UTC 5 July, the MCS had taken on a prominent bowing structure and had crossed into eastern Ohio. The P-3 conducted a spiral between 0040 and 0012 UTC in the ESR behind the apex of the bow. The MCS began to weaken by 0130 UTC, and a final spiral was executed within the ESR between 0137 and 0158 UTC. This MCS is discussed further by Wheatley et al. (2006).

o. 6 July 2003: BAMEX IOP18

During BAMEX IOP 18, the P-3 initially targeted a developing MCS immediately to the north of the Iowa–Missouri border. A single spiral was conducted in the AR behind the formative ESR of this MCS between 0319 and 0327 UTC 6 July 2003. The P-3 then shifted to northeastern Nebraska, where a bowing TS MCS had evolved in an unstable and moist environment. Two separate spirals were conducted within the ESR behind the apex of the bow, one between 0529 and 0542 UTC and another between 0638 and 0647 UTC, with each transecting the RIJ. Numerous studies have addressed this Nebraska MCS, including Wakimoto et al. (2006a,b), Wheatley et al. (2006), Wheatley and Trapp (2008), and Davis and Galarneau (2009).

REFERENCES

Alfonso, A. P., and L. R. Naranjo, 1996: The 13 March 1993 severe squall line over western Cuba. *Wea. Forecasting*, **11**, 89–102, https://doi.org/10.1175/1520-0434(1996)011<0089:TMSSLO>2.0.CO;2.

Biggerstaff, M. I., and R. A. Houze Jr., 1991: Kinematic and precipitation structure of the 10–11 June 1985 squall line. *Mon. Wea. Rev.*, **119**, 3034–3065, https://doi.org/10.1175/1520-0493(1991)119<3034:KAPSOT>2.0.CO;2.

——, and ——, 1993: Kinematics and microphysics of the transition zone of the 10–11 June 1985 squall line. *J. Atmos. Sci.*, **50**, 3091–3110, https://doi.org/10.1175/1520-0469(1993)050<3091:KAMOTT>2.0.CO;2.

Bodine, D. J., and K. L. Rasmussen, 2017: Evolution of mesoscale convective system organizational structure and convective line propagation. *Mon. Wea. Rev.*, **145**, 3419–3440, https://doi.org/10.1175/MWR-D-16-0406.1.

Brandes, E. A., K. Ikeda, G. Zhang, M. Schönhuber, and R. M. Rasmussen, 2007: A statistical and physical description of hydrometeor distributions in Colorado snowstorms using a video disdrometer. *J. Appl. Meteor. Climatol.*, **46**, 634–650, https://doi.org/10.1175/JAM2489.1.

——, ——, G. Thompson, and M. Schönhuber, 2008: Aggregate terminal velocity/temperature relations. *J. Appl. Meteor. Climatol.*, **47**, 2729–2736, https://doi.org/10.1175/2008JAMC1869.1.

Cunning, J. B., 1986: The Oklahoma-Kansas Preliminary Regional Experiment for STORM-Central. *Bull. Amer. Meteor. Soc.*, **67**, 1478–1486, https://doi.org/10.1175/1520-0477(1986)067<1478:TOKPRE>2.0.CO;2.

Davis, C. A., and S. B. Trier, 2007: Mesoscale convective vortices observed during BAMEX. Part I: Kinematic and thermodynamic structure. *Mon. Wea. Rev.*, **135**, 2029–2049, https://doi.org/10.1175/MWR3398.1.

——, and T. J. Galarneau, 2009: The vertical structure of mesoscale convective vortices. *J. Atmos. Sci.*, **66**, 686–704, https://doi.org/10.1175/2008JAS2819.1.

——, and Coauthors, 2004: The Bow Echo and MCV Experiment: Observations and opportunities. *Bull. Amer. Meteor. Soc.*, **85**, 1075–1094, https://doi.org/10.1175/BAMS-85-8-1075.

Field, P. R., and A. J. Heymsfield, 2003: Aggregation and scaling of ice crystal size distributions. *J. Atmos. Sci.*, **60**, 544–560, https://doi.org/10.1175/1520-0469(2003)060<0544:AASOIC>2.0.CO;2.

——, ——, and A. Bansemer, 2006: A test of ice self-collection kernels using aircraft data. *J. Atmos. Sci.*, **63**, 651–666, https://doi.org/10.1175/JAS3653.1.

Finlon, J. A., G. M. McFarquhar, S. W. Nesbitt, R. M. Rauber, H. Morrison, W. Wu, and P. Zhang, 2019: A novel approach for characterizing the variability in mass–dimension relationships: Results from MC3E. *Atmos. Chem. Phys.*, **19**, 3621–3643, https://doi.org/10.5194/acp-19-3621-2019.

Flournoy, M. D., and M. C. Coniglio, 2019: Origins of vorticity in a simulated tornadic mesovortex observed during PECAN on 6 July 2015. *Mon. Wea. Rev.*, **147**, 107–134, https://doi.org/10.1175/MWR-D-18-0221.1.

Gallus, W. A., N. A. Snook, and E. V. Johnson, 2008: Spring and summer severe weather reports over the Midwest as a function

of convective mode: A preliminary study. *Wea. Forecasting*, **23**, 101–113, https://doi.org/10.1175/2007WAF2006120.1.

Geerts, B., and Coauthors, 2017: The 2015 Plains Elevated Convection at Night field project. *Bull. Amer. Meteor. Soc.*, **98**, 767–786, https://doi.org/10.1175/BAMS-D-15-00257.1.

Grim, J. A., G. M. McFarquhar, R. M. Rauber, A. M. Smith, and B. F. Jewett, 2009a: Microphysical and thermodynamic structure and evolution of the trailing stratiform regions of mesoscale convective systems during BAMEX. Part II: Column model simulations. *Mon. Wea. Rev.*, **137**, 1186–1205, https://doi.org/10.1175/2008MWR2505.1.

——, R. M. Rauber, G. M. McFarquhar, B. F. Jewett, and D. P. Jorgensen, 2009b: Development and forcing of the rear inflow jet in a rapidly developing and decaying squall line during BAMEX. *Mon. Wea. Rev.*, **137**, 1206–1229, https://doi.org/10.1175/2008MWR2503.1.

Gu, Y., and K. N. Liou, 2000: Interactions of radiation, microphysics, and turbulence in the evolution of cirrus clouds. *J. Atmos. Sci.*, **57**, 2463–2479, https://doi.org/10.1175/1520-0469(2000)057<2463:IORMAT>2.0.CO;2.

Helmus, J. J., and S. M. Collis, 2016: The Python ARM Radar Toolkit (Py-ART), a library for working with weather radar data in the Python programming language. *J. Open Res. Software*, **4**, e25, https://doi.org/10.5334/jors.119.

Heymsfield, A. J., P. R. Field, M. Bailey, D. Rogers, J. Stith, C. Twohy, Z. Wang, and S. Haimov, 2011: Ice in Clouds Experiment—Layer Clouds. Part I: Ice growth rates derived from lenticular wave cloud penetrations. *J. Atmos. Sci.*, **68**, 2628–2654, https://doi.org/10.1175/JAS-D-11-025.1.

Hitchcock, S. M., R. S. Schumacher, G. R. Herman, M. C. Coniglio, M. D. Parker, and C. L. Ziegler, 2019: Evolution of pre-and postconvective environmental profiles from mesoscale convective systems during PECAN. *Mon. Wea. Rev.*, **147**, 2329–2354, https://doi.org/10.1175/MWR-D-18-0231.1.

Houze, R. A., Jr., M. I. Biggerstaff, S. A. Rutledge, and B. F. Smull, 1989: Interpretation of Doppler weather radar displays of midlatitude mesoscale convective systems. *Bull. Amer. Meteor. Soc.*, **70**, 608–619, https://doi.org/10.1175/1520-0477(1989)070<0608:IODWRD>2.0.CO;2.

Jackson, R. C., and Coauthors, 2012: The dependence of ice microphysics on aerosol concentration in Arctic mixed-phase stratus clouds during ISDAC and M-PACE. *J. Geophys. Res.*, **117**, D15207, https://doi.org/10.1029/2012JD017668.

——, G. M. McFarquhar, J. L. Stith, M. Beals, R. A. Shaw, J. Jensen, J. Fugal, and A. V. Korolev, 2014: An assessment of the impact of antishattering tips and artifact removal techniques on cloud ice size distributions measured by the 2D cloud probe. *J. Atmos. Oceanic Technol.*, **31**, 2567–2590, https://doi.org/10.1175/JTECH-D-13-00239.1.

James, E. P., and R. H. Johnson, 2010: Patterns of precipitation and mesolow evolution in midlatitude mesoscale convective vortices. *Mon. Wea. Rev.*, **138**, 909–931, https://doi.org/10.1175/2009MWR3076.1.

Jensen, M. P., and Coauthors, 2016: The Midlatitude Continental Convective Clouds Experiment (MC3E). *Bull. Amer. Meteor. Soc.*, **97**, 1667–1686, https://doi.org/10.1175/BAMS-D-14-00228.1.

Keene, K. M., and R. S. Schumacher, 2013: The bow and arrow mesoscale convective structure. *Mon. Wea. Rev.*, **141**, 1648–1672, https://doi.org/10.1175/MWR-D-12-00172.1.

Korolev, A. V., and G. A. Isaac, 2005: Shattering during sampling by OAPs and HVPS. Part I: Snow particles. *J. Atmos. Oceanic Technol.*, **22**, 528–542, https://doi.org/10.1175/JTECH1720.1.

Kumjian, M. R., Y. P. Richardson, T. Meyer, K. A. Kosiba, and J. Wurman, 2018: Resonance scattering effects in wet hail observed with a dual-X-band-frequency, dual-polarization Doppler on Wheels radar. *J. Appl. Meteor. Climatol.*, **57**, 2713–2731, https://doi.org/10.1175/JAMC-D-17-0362.1.

Lin, G., B. Geerts, Z. Wang, C. Grasmick X. Jing, and J. Yang, 2019: Interactions between a nocturnal MCS and the stable boundary layer as observed by an airborne compact Raman lidar during PECAN. *Mon. Wea. Rev.*, **147**, 3169–3189, https://doi.org/10.1175/MWR-D-18-0388.1.

McFarquhar, G. M., and A. J. Heymsfield, 1996: Microphysical characteristics of three anvils sampled during the Central Equatorial Pacific Experiment. *J. Atmos. Sci.*, **53**, 2401–2423, https://doi.org/10.1175/1520-0469(1996)053<2401:MCOTAS>2.0.CO;2.

——, M. S. Timlin, R. M. Rauber, B. F. Jewett, J. A. Grim, and D. P. Jorgensen, 2007a: Vertical variability of cloud hydrometeors in the stratiform region of mesoscale convective systems and bow echoes. *Mon. Wea. Rev.*, **135**, 3405–3428, https://doi.org/10.1175/MWR3444.1.

——, G. Zhang, M. R. Poellot, G. L. Kok, R. McCoy, T. Tooman, A. Fridlind, and A. J. Heymsfield, 2007b: Ice properties of single-layer stratocumulus during the Mixed-Phase Arctic Cloud Experiment: 1. Observations. *J. Geophys. Res.*, **112**, D24201, https://doi.org/10.1029/2007JD008633.

——, and Coauthors, 2011: Indirect and Semi-Direct Aerosol Campaign: The impact of Arctic aerosols on clouds. *Bull. Amer. Meteor. Soc.*, **92**, 183–201, https://doi.org/10.1175/2010BAMS2935.1.

Melhauser, C., and F. Zhang, 2012: Practical and intrinsic predictability of severe and convective weather at the mesoscales. *J. Atmos. Sci.*, **69**, 3350–3371, https://doi.org/10.1175/JAS-D-11-0315.1.

Parker, M. D., and R. H. Johnson, 2000: Organizational modes of midlatitude mesoscale convective systems. *Mon. Wea. Rev.*, **128**, 3413–3436, https://doi.org/10.1175/1520-0493(2001)129<3413:OMOMMC>2.0.CO;2.

Przybylinski, R. W., 1995: The bow echo: Observations, numerical simulations, and severe weather detection methods. *Wea. Forecasting*, **10**, 203–218, https://doi.org/10.1175/1520-0434(1995)010<0203:TBEONS>2.0.CO;2.

Smith, A. M., G. M. McFarquhar, R. M. Rauber, J. A. Grim, M. S. Timlin, B. F. Jewett, and D. P. Jorgensen, 2009: Microphysical and thermodynamic structure and evolution of the trailing stratiform regions of mesoscale convective systems during BAMEX. Part I: Observations. *Mon. Wea. Rev.*, **137**, 1165–1185, https://doi.org/10.1175/2008MWR2504.1.

Smull, B. F., and R. A. Houze, 1985: A midlatitude squall line with a trailing region of stratiform rain: Radar and satellite observations. *Mon. Wea. Rev.*, **113**, 117–133, https://doi.org/10.1175/1520-0493(1985)113<0117:AMSLWA>2.0.CO;2.

Stechman, D. M., G. M. McFarquhar, R. M. Rauber, M. M. Bell, B. F. Jewett, and J. Martinez, 2020: Spatiotemporal evolution of the microphysical and thermodynamic characteristics of the 20 June 2015 PECAN MCS. *Mon. Wea. Rev.*, **148**, 1363–1388, https://doi.org/10.1175/MWR-D-19-0293.1.

Storm, B. A., M. D. Parker, and D. P. Jorgensen, 2007: A convective line with leading stratiform precipitation from BAMEX. *Mon. Wea. Rev.*, **135**, 1769–1785, https://doi.org/10.1175/MWR3392.1.

Strapp, J. W., J. D. MacLeod, and L. E. Lilie, 2008: Calibration of ice water content in a wind tunnel/engine test cell facility. *15th Int. Conf. on Clouds and Precipitation*, Cancun, Mexico,

International Commission on Clouds and Precipitation, P13.1, http://cabernet.atmosfcu.unam.mx/ICCP-2008/abstracts/Program_on_line/Poster_13/StrappEtAl-extended.pdf.

Wakimoto, R. M., H. V. Murphey, C. A. Davis, and N. T. Atkins, 2006a: High winds generated by bow echoes. Part II: The relationship between the mesovortices and damaging straight-line winds. *Mon. Wea. Rev.*, **134**, 2813–2829, https://doi.org/10.1175/MWR3216.1.

——, ——, A. Nester, D. P. Jorgensen, and N. T. Atkins, 2006b: High winds generated by bow echoes. Part I: Overview of the Omaha bow echo 5 July 2003 storm during BAMEX. *Mon. Wea. Rev.*, **134**, 2793–2812, https://doi.org/10.1175/MWR3215.1.

——, P. Stauffer, and W.-C. Lee, 2015: The vertical vorticity structure within a squall line observed during BAMEX: Banded vorticity features and the evolution of a bowing segment. *Mon. Wea. Rev.*, **143**, 341–362, https://doi.org/10.1175/MWR-D-14-00246.1.

Weisman, M. L., 2001: Bow echoes: A tribute to T. T. Fujita. *Bull. Amer. Meteor. Soc.*, **82**, 97–116, https://doi.org/10.1175/1520-0477(2001)082<0097:BEATTT>2.3.CO;2.

Wheatley, D. M., and R. J. Trapp, 2008: The effect of mesoscale heterogeneity on the genesis and structure of mesovortices within quasi-linear convective systems. *Mon. Wea. Rev.*, **136**, 4220–4241, https://doi.org/10.1175/2008MWR2294.1.

——, ——, and N. T. Atkins, 2006: Radar and damage analysis of severe bow echoes observed during BAMEX. *Mon. Wea. Rev.*, **134**, 791–806, https://doi.org/10.1175/MWR3100.1.

Wu, W., and G. M. McFarquhar, 2016: On the impacts of different definitions of maximum dimension for nonspherical particles recorded by 2D imaging probes. *J. Atmos. Oceanic Technol.*, **33**, 1057–1072, https://doi.org/10.1175/JTECH-D-15-0177.1.

Zipser, E. J., R. J. Meitín, and M. A. LeMone, 1981: Mesoscale motion fields associated with a slowly moving GATE convective band. *J. Atmos. Sci.*, **38**, 1725–1750, https://doi.org/10.1175/1520-0469(1981)038<1725:MMFAWA>2.0.CO;2.